40th Fluid Dynamics Conference and Exhibit
28 June - 1 July 2010, Chicago, Illinois

AIAA 2010-5004

Instability and Transition on the HIFiRE-5 in a Mach-6 Quiet Tunnel

Thomas J. Juliano *
and Steven P. Schneider †
School of Aeronautics and Astronautics, Purdue University, West Lafayette, IN 47907-1282

A 2:1 aspect-ratio elliptic cone was tested in the Boeing/AFOSR Mach-6 Quiet Tunnel to investigate the effects of freestream noise level, surface roughness, angle of attack, and freestream Reynolds number on boundary layer transition on the windward surface. The cone had a minor axis half-angle of 7° and a nose radius of 0.95 mm. Temperature-sensitive paint enabled a global measurement of the temperature distribution and detection of the transition front. Two modes of transition were observed: transition along the centerline, suspected to arise from the amplification of second-mode waves in the inflected boundary layer, and transition roughly halfway between the centerline and leading edges, probably due to the breakdown of crossflow vortices. Reducing noise level from conventional (root-mean-square pressure 3% of the mean) to quiet (root-mean-square pressure less than 0.1% of the mean) substantially delayed both transition modes. Increasing the angle of attack from 0° to 4° delayed the crossflow transition mode on the windward side. Transition moved forward as freestream unit Reynolds number increased from $2.6{\cdot}10^6$ /m to $11.9{\cdot}10^6$ /m. PCB fast-response pressure transducers installed along the model centerline detected apparent instabilities at frequencies from 50 to 150 kHz prior to transition under noisy flow.

Nomenclature

e	ellipse aspect ratio; $e = 2.0$ for the HIFiRE-5
I	temperature sensitive paint intensity
L	model length
M	freestream Mach number
p	pressure
Re	freestream unit Reynolds number
Re_x	Reynolds number based on length x and freestream conditions
T	temperature
t	time
u	streamwise velocity (parallel to x)
v	spanwise velocity (parallel to y)
x	axial distance parallel to model centerline
y	spanwise distance
z	vertical distance from model surface
α	angle of attack
ρ	density

Subscripts

0	stagnation
i	initial
∞	freestream
dark	without illumination
off	flow off (before the tunnel run)
on	flow on (while the tunnel is running)
ref	reference
wall	at the model wall

*Research Assistant. Student Member, AIAA.
†Professor. Associate Fellow, AIAA.

I. HIFiRE

The Hypersonic International Flight Research and Experimentation (HIFiRE) program is a joint effort of the U.S. Air Force Research Laboratory (AFRL) and the Australian Defence Science and Technology Organization (DSTO).[1] Its purpose is to develop and validate technologies critical to next generation hypersonic aerospace systems. To this end, a coordinated set of computational, ground, and flight tests are planned.

The HIFiRE program is organized as a collection of up to ten research projects, each of which has a unique subset of goals regarding aerodynamics, propulsion, navigation, control, materials, and others. Aerothermodynamics, including boundary-layer transition, is a primary goal of the HIFiRE-1 and -5 tests. HIFiRE-1, a cone-cylinder-flare geometry, examined natural and roughness-induced transition.[2–4] Tests in the BAM6QT showed a significant transition delay under quiet flow, reinforcing the necessity of quiet-flow testing as a component of transition studies.[5]

The second HIFiRE test examining boundary-layer stability and transition is HIFiRE-5. An elliptic cone was chosen as the geometry because of its resemblance to practical geometries, the body of previous work on such shapes, and the presence of three-dimensional flow. The HIFiRE-5 has a small bluntness nosetip (2.5 mm nose radius) to moderate heating. Three-dimensional flow introduces transition mechanisms not present in axisymmetric or two-dimensional flow.

II. Laminar-to-Turbulent Transition and Quiet Flow

Fluid flow in a boundary layer can exist in two regimes, laminar and turbulent, usually separated by a transitional phase. In natural transition, disturbances in the laminar flow, such as free-stream turbulence, free-stream vorticity disturbances, or surface roughness, are amplified through various instabilities and lead to transition to turbulent flow.[6] Larger initial disturbances will bypass the linear growth mechanisms and lead directly to turbulent flow.

The streamlines of particles in a laminar boundary layer are smoother and straighter than those in turbulent flow and result in less friction and heat flux at the wall.[7] The prediction and control of transition is an important factor in the design of hypersonic vehicles due to its effect on surface heating, skin friction, separation, aero-optical distortion, and other boundary-layer properties.[8] This issue is especially pressing at hypersonic velocities due to the high energies and heating involved.

Many factors influence transition, including Reynolds number, surface roughness, and atmospheric conditions such as freestream noise level.[6,9] The noise level of a flow can be defined as the ratio of root-mean-square (rms) pitot stagnation pressure to mean pitot stagnation pressure. Atmospheric levels are typically $< 0.05\%$.[10] Such low levels are regarded as "quiet". Accurate wind-tunnel testing requires matching as many flight parameters as possible, but achieving this low noise level in a wind tunnel has been particularly difficult.[11] Conventional tunnels have noise levels of 1–3%. Reference 12 contains a thorough discussion of the influence of tunnel noise on boundary-layer transition. The higher noise levels in a conventional ground-test facility have been shown to lead to early transition as well as to changes in the parametric trends of transition. Thus, ground tests in a quiet tunnel are necessary in order to obtain more accurate transition estimates.[13]

III. Selected Previous Work with Elliptic Cones

Elliptic cones have been the subject of several previous studies of three-dimensional hypersonic flow. The three-dimensional flowfield arising from the non-axisymmetric geometry introduces crossflow as an additional transition mode that may dominate under certain conditions. Improved understanding of all the relevant transition modes is essential to the prediction of transition on complicated geometries, which in turn is an important facet of future designs.

A. AEDC Tunnel B

Kimmel and Poggie tested a sharp elliptic cone in the Arnold Engineering Development Center von Karman Facility Tunnel B at Mach 8.[14,15] The nose radius was 0.4 mm, the cross section aspect ratio e was 2:1, and the half angle along the minor axis was 7°. The model overall length L was 1.016 m. The majority of their data were collected at $Re = 1.79 \cdot 10^6$ /m and $x/L = 0.8$, so $Re_x = 1.6 \cdot 10^6$. Hot-film probes with constant-

current anemometers were used to measure boundary-layer disturbance frequencies and amplitudes. Oil flow and schlieren provided flow visualization. The oil flow provided evidence of transition near the centerline as well as crossflow between the leading edges and centerline that had not yet led to turbulence.

Parabolized Navier-Stokes and linear stability computations were made in support of these measurements. Three different aspect ratios — 1.5, 2, and 4:1 — were computed. The maximum N-factor for the $e = 1.5$ geometry was less than 5, making transition unlikely. For $e = 4$, crossflow amplification N reached 5 at $x/L = 0.3$. Thus early transition was possible, which would make it difficult to probe the laminar and transitional boundary layer. Therefore, the 2:1 configuration was chosen for further computational as well as experimental study.

The hot-film probes were able to detect disturbances over a range of azimuths. Low frequency ($f \approx$ 20 kHz) peaks were associated with crossflow instability, whereas higher frequency (80 kHz) peaks match the predicted frequency of second-mode instability. Broadband noise replaced the peaks at azimuths near the centerline, which corroborated the oil flow and heat-transfer gauges indicating a turbulent boundary layer.

B. Princeton Mach 8 Facility

Huntley and Smits conducted numerous flow visualization experiments on sharp 2:1 and 4:1 elliptic cones at the Princeton Mach 8 Facility.[16,17] The minor axis half-angle θ was 9° for the 4:1 elliptic cone, compared to 7° for the Tunnel B tests and the HIFiRE-5. The model length was 0.242 m and the nominal nose radius was 200 μm on the major axis. Freestream Reynolds number ranged from 2.0 to $21 \cdot 10^6$ /m.

Remarkable images of boundary-layer instability and transition along the model centerline were obtained with Filtered Rayleigh Scattering in the centerline plane (Figure 4 in Ref. 16). Prior to transition, traveling waves of density fluctuations with a wavelength 4–5 times the boundary layer thickness were imaged. Waves with such a long wavelength are unlikely to have been second-mode waves. At higher Re nearer to transition onset, the fluctuation wavelength decreased to twice the boundary layer thickness, which agrees with the measurements in Tunnel B as well as theoretical predictions for second-mode waves.

The same technique was used to image the boundary layer in a plane perpendicular to the model axis (Figure 5 in Ref. 16). The centerline ballooning of the boundary layer predicted by the computations of Kimmel et al. was observed.[18] As Re was increased to $6.5–8.0 \cdot 10^6$ /m, vortical structures were visible on either side of the centerline bulge. At yet higher $Re = 10.5 \cdot 10^6$ /m, flow near the centerline was late-transitional, and vortices had begun to develop further from the centerline.

Similar results were observed for the 2:1 elliptic cone. They were inclined more toward the centerline for the 4:1 than the 2:1 aspect ratio, which was attributed to the stronger crossflow for the higher eccentricity cross section.

C. Purdue Quiet-Flow Ludwieg Tube

Schmisseur et al. tested a 4:1 elliptic cone in the Purdue Quiet-Flow Ludwieg Tube at Mach 4.[19,20] The major and minor axes at the base were 80 and 20 mm, respectively. The minor-axis half-angle was 4.5° and the nose radius was less than 0.051 mm along the minor axis. The primary goal of these tests was to investigate boundary-layer receptivity with controlled perturbations from a thermal spot generated by a pulsed laser. Constant-temperature and constant-current hot wires were used to probe the flowfield away the cone and a hot-film array provided surface measurements.

The surface hot films nearest the minor axis (7 mm from the centerline) indicated the strongest response to the laser perturber. Two possible explanations for this finding were provided. One suggestion is that the crossflow convects the disturbance towards the centerline, concentrating the disturbance near the centerline. The other explanation is that the boundary layer above the minor axis is less stable than elsewhere around the elliptic cone.

Mean-flow mass-flux profiles from calibrated hot wires are presented in Reference 20. The hot wires indicate a highly inflected mass-flux profile above the centerline with a very steep velocity gradient near the outer edge of the boundary layer.

These measurements were supported by mean-flow and stability computations by Lyttle and Huang et al.[21,22] Lyttle applied the crossflow transition correlation developed by Reed and Haynes in Reference 23 and found that transition would not be expected for the conditions in the Mach-4 Tunnel for $e = 2$, 3, or 4. Huang et al. reached the opposite conclusion from their PSE computations: using $N = 10$ as the transition

threshold, transition is predicted to occur for the 4:1 elliptical cone. They found that a stationary crossflow vortex was the most unstable.

D. Computational Results for the HIFiRE-5

Computational analysis of the HIFiRE-5 was conducted for selected wind tunnel test cases as well as the proposed flight conditions.[24,25] Among the cases tested were two simulating the HIFiRE-5 at 0 and 4° angle of attack in the BAM6QT near the maximum quiet pressure achieved at that time (970 kPa in December 2008). Unsurprisingly, the computations predict many of the same interesting flow features encountered in the experiments discussed above.

These computations were made by Meelan Choudhari and Jeff White of the NASA Langley Computational Aerosciences Branch using VULCAN. They supersede preliminary results obtained with LAURA. The following flow conditions were selected: freestream $M = 6.0$, $p_0 = 970$ kPa, $T_0 = 433$ K, $Re = 10.2 \cdot 10^6$ /m, and model wall $T = 300$ K. These parameters were the same for both the 0° and 4° angle of attack cases. The computational domain was extended to $x = 381$ mm (the model length is 328 mm) to mitigate the effects of the outflow boundary condition.

Dr. Choudhari provided these data directly to the author. These figures were then created from those data.

Figure 1 shows the static pressure 20 gridpoints (0.076 mm) above the surface of the HIFiRE-5 at $\alpha = 0°$. Only one quarter of the surface is shown, from leading edge to centerline. The units shown in the legend are Pascals. The crossflow-inducing spanwise pressure gradient is clear. The pressure along the leading edges is twice that along the centerline. It arises from the azimuthal variation in the shock angle around the elliptic cone. The pressure in the vicinity of the blunt nosetip is high for the same reason — the flow there has passed through the nearly-normal detached shock ahead of the tip. Several streamlines exhibiting the spanwise velocity component within the boundary layer are shown as well.

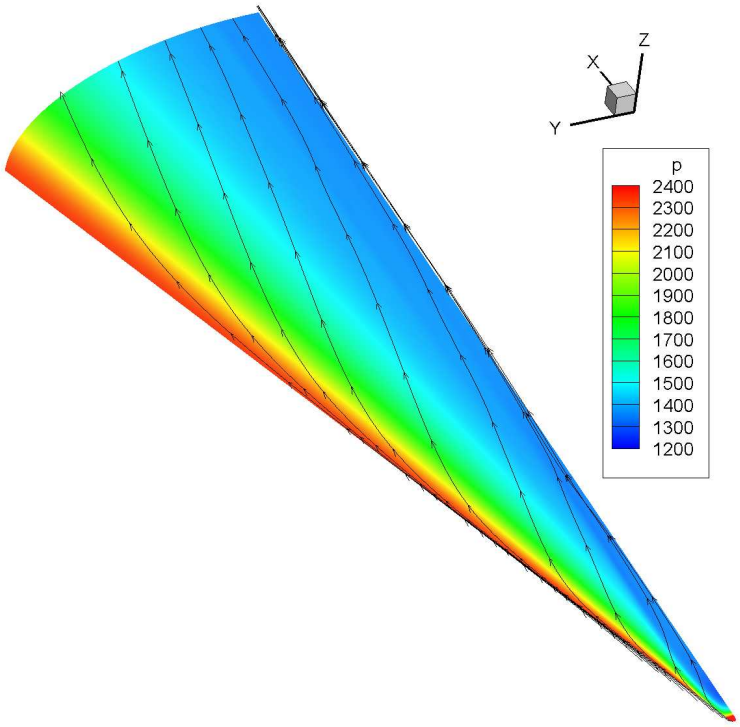

Figure 1: CFD prediction of static pressure and selected streamlines for $\alpha = 0°$. Units are Pa. Computation by M. Choudhari and J. White

Figure 2 presents the computed stagnation temperature T_0 near the surface, streamwise velocity u, and a few streamlines for $\alpha = 0°$. The temperature units are K, and u is in m/s. The T_0 contour shows the data for 40 gridpoints (0.18 mm) above the surface. These data are useful because they are qualitatively similar to

the output from Temperature-Sensitive Paint. The spanwise slices (showing u) occur every 50 mm starting at $x = 50$ mm. The data in the immediate vicinity of the nosetip was suppressed to reduce the computer memory needed to display these contours.

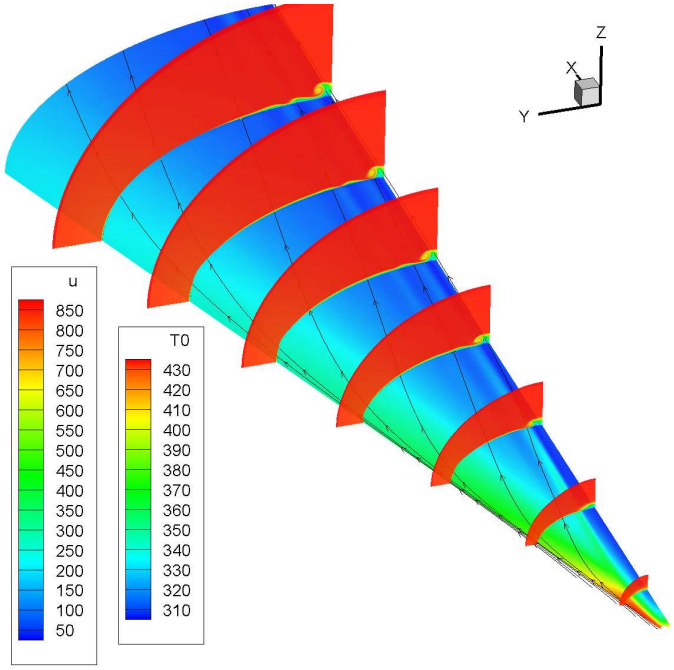

Figure 2: CFD prediction of surface stagnation temperature T_0, streamwise velocity u, and selected streamlines for $\alpha = 0°$. Surface contour is T_0 in K and spanwise slices show u in m/s. Computation by M. Choudhari and J. White

One significant effect of the crossflow is the accumulation of low-momentum fluid near the HIFiRE-5 centerline, as shown by the velocity contours. A vortex is predicted to form on each side of this bulge. In an approximate and qualitative way, these results resemble those from the literature.

The thick boundary layer near the centerline substantially reduces the heat flux into the wall because of the reduced temperature gradient. This reduced heating is apparent in the near-surface T_0 contour and figures prominently in the TSP data presented in Section VIII. The vortices on either side of the centerline bulge convect high-momentum fluid closer to the wall, thereby thinning the boundary layer and increasing the heat flux. These off-centerline hot streaks are even more prominent at $\alpha = 4°$.

IV. The Boeing/AFOSR Mach-6 Quiet Tunnel

The Boeing/AFOSR Mach-6 Quiet Tunnel (BAM6QT) at Purdue University is one of two hypersonic quiet tunnels in operation anywhere in the world, and the only one offering optical access to the test section. In order to minimize complexity and cost, a Ludwieg-tube design was chosen for the BAM6QT. A Ludwieg tube is a high-pressure driver tube connected to a converging-diverging nozzle that accelerates the flow to the desired Mach number, which is set by the ratio between the test section and throat areas.[26] The tunnel configuration is shown in Figure 3. The maximum stagnation pressure for the BAM6QT is 2.0 MPa, although the design maximum quiet pressure is 1.0 MPa. This goal was not achieved until November 2006.[27] While running quietly, the noise level is less than 0.05%, and it increases to about 3% when noisy.[28]

Air entering the driver tube and the driver tube itself are heated to a nominal temperature of 433 K (160 °C) to avoid nitrogen liquefaction in the nozzle, where the static temperature decreases to 53 K when expanded to Mach 6.

The BAM6QT employs many features to maintain a laminar nozzle-wall boundary layer, thereby achieving quiet flow.[28] Among these features is a suction slot upstream of the throat that removes the boundary layer on the contraction, allowing a fresh laminar boundary layer to grow on the expanding portion of the nozzle. In order to run quietly, a valve must be opened connecting the bleed slot to the vacuum tank.

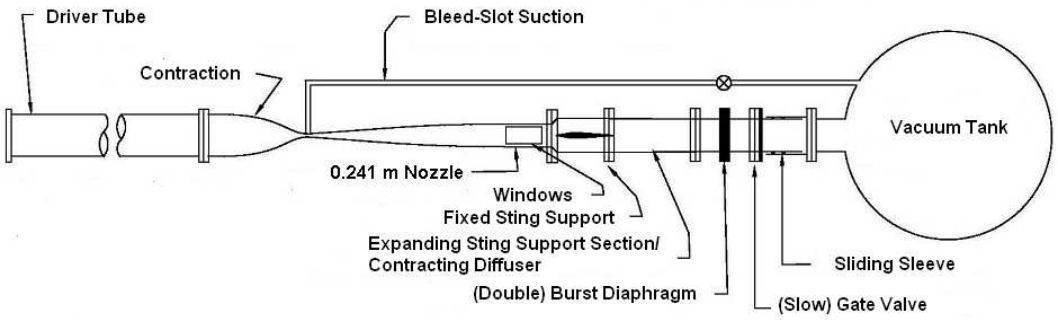

Figure 3: BAM6QT schematic

Thus, the BAM6QT can be run with a conventional noise level by leaving the bleed line closed. A more comprehensive discussion of the components of the BAM6QT is contained in Reference 29.

The nozzle-wall boundary layer is more likely to transition to turbulent (resulting in noisy flow) at higher stagnation pressures. For the results herein, the maximum quiet pressure was consistently above 1000 kPa.

At the time that HIFiRE-5 testing was performed, the run duration was about 6 s for quiet flow (with the contraction bleed lines open) and 10 s for noisy flow (bleed lines closed). The increased mass flux through the bleed lines results in a faster emptying of the driver tube and decreased run time for quiet-flow testing. The run time also depends on the efficiency of the diffuser; HIFiRE-5 tests were conducted with the second-generation sting-support section and diffuser described in Reference 30. The pipe insert was installed in the sting-support section, with no gap between it and the test section. The pipe insert extension described in Reference 31 was also installed for most tests because it was found to inhibit separation of the nozzle-wall boundary layer.

A. Test Section

Figure 4 shows Section 8, the last nozzle section. The region of useful quiet flow lies between the characteristics marking the onset of uniform flow and the characteristics marking the upstream boundary of acoustic radiation from the onset of turbulence in the nozzle-wall boundary layer. A 7.5° half-angle sharp cone is drawn on the figure. The rectangles are drawn on the nozzle at the location of window openings.

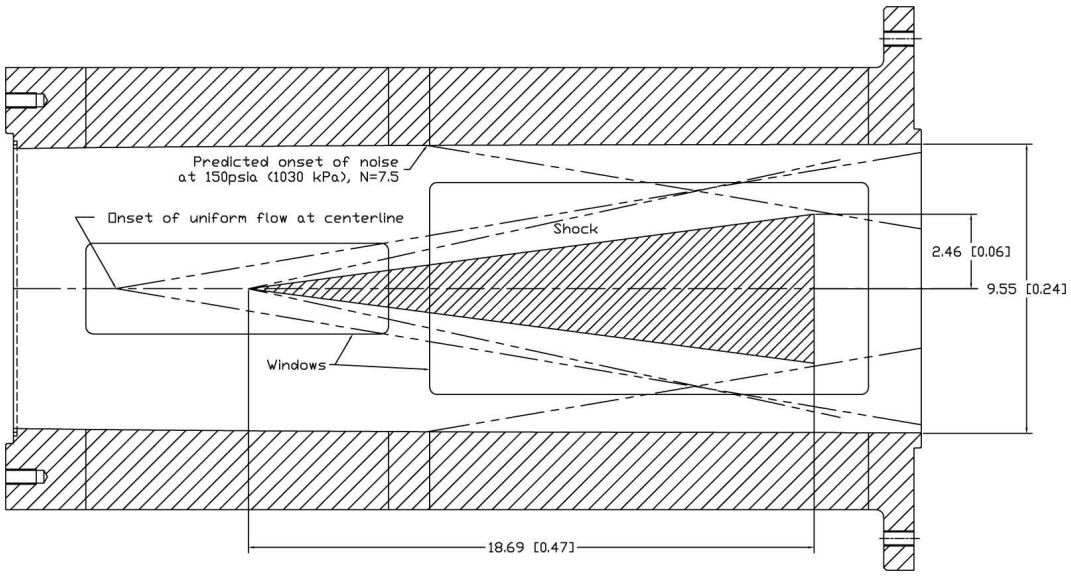

Figure 4: Schematic of Mach-6 quiet nozzle with 7.5° cone model. Dimensions are inches [meters].

Section 8 has several ports for various instruments and windows. A large acrylic window was used for most HIFiRE-5 temperature-sensitive-paint tests because the model was large enough to benefit from the good field of view (see Section VI). A hot-film array was installed in the forward-lower or a forward-side port. During every run, the uncalibrated output from the nozzle-wall hot-films were recorded in order to verify whether the flow was noisy, quiet, or separated.[27,29,32,33] Reference 34 contains more details about these measurements.

B. Extent of Quiet Flow

A careful characterization of the quality, extent, and uniformity of quiet flow in the BAM6QT test section has not been conducted since quiet-flow operation at high freestream Reynolds number ($Re > 10.7 \cdot 10^6$ /m, $p_0 > 1000$ kPa) was achieved in September 2006. Measuring the extent of the quiet-flow test core is a special concern for the HIFiRE-5 because it was far back in the test section to inhibit separation and its semi-major axis was larger than the radius of most models typically run in the tunnel (82 mm, compared to 70 mm for a large circular cone). The radius at the exit of the test section is 120 mm, so the model is as close as 38 mm to the tunnel wall.It is thus a distinct possibility that the noise level near the tunnel centerline would be low (with its origin upstream of nozzle-wall boundary-layer transition) while the back of the model is exposed to high noise radiated from a turbulent boundary layer.

There is evidence that higher noise emanating from a turbulent nozzle-wall boundary layer can be seen in the temperature-sensitive paint data. The TSP instrumentation and data reduction is described in detail in Section VI. Figure 5 shows two TSP images from a run that demonstrated a transient flow quality issue. At $t = 0.65$ s after startup, the lower corner of the model shows a temperature increase, presumably due to transition on the model boundary layer (Figure 5a). A similar increase is not observed on the upper corner. Later, at $t = 2.8$ s, the image is essentially symmetric, as expected (Figure 5b).

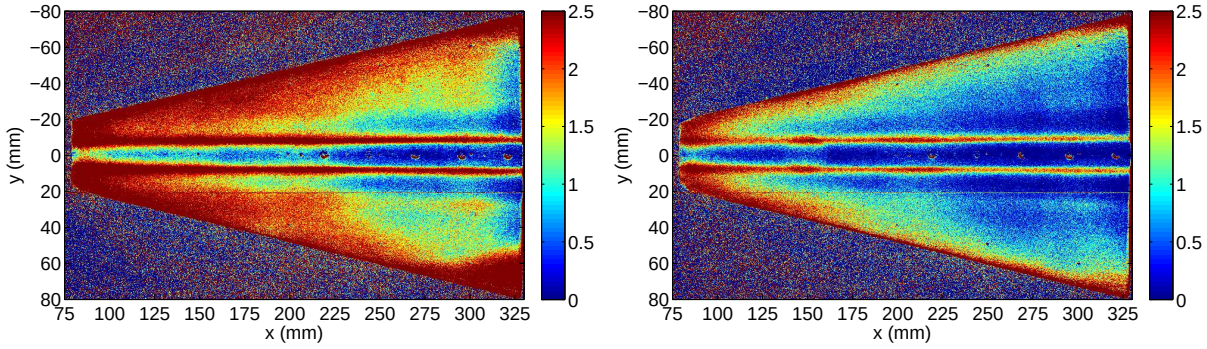

(a) $t = 0.65$ s (b) $t = 2.80$ s

Figure 5: Impact of flow quality on TSP results. Contraction bleed open, nominal $M = 6.0$, $\alpha = 4°$, $Re_i = 10.4 \cdot 10^6$ /m, $p_{0i} = 970$ kPa, $T_{0i} = 432$ K

It appears that a disturbance occasionally develops far downstream in the nozzle. The higher noise leads to transition on the HIFiRE-5, which is detected by TSP. Seeing and avoiding the data corrupted by the higher noise level may be a simple and effective means of dealing with this disturbance.

However, it is also possible that this far-downstream disturbance affects the model boundary layer in a subtler way. Perhaps the transition that is observed under nominally quiet flow (contraction bleed valve open and stagnation pressure less than the maximum quiet pressure) is in fact promoted by higher noise levels that may be present on the downstream ends of the model. *Thus, the quiet-flow transition results should be regarded as under 'presumed' or 'nominally' quiet flow.*

V. HIFiRE-5 Model

The HIFiRE-5 model tested in the BAM6QT was designed by the author during May–July 2008 to match the geometry provided by Dr. Roger Kimmel, the HIFiRE-5 principal investigator. The scale of the model tested in the BAM6QT was chosen to be 38.1% to match the model tested at the NASA Langley Research Center. Only the first 861 mm of the full-scale vehicle is modeled (model length $L = 328$ mm). The full

vehicle has an elliptical-to-circular adapter at this location to fair the elliptic cone to the 355.6-mm-diameter sounding rocket, but this portion is omitted from the BAM6QT model so that the model was not too long for the test section. The base semi-major axis is 82 mm, the base semi-minor axis is 41 mm, the length from nosetip to base is 328 mm, and the nosetip radius along the minor axis is 0.95 mm.

The model has numerous features that allow testing for different configurations and several sensors (Figure 6). The flight vehicle will have a break between the nosetip and frustum at approximately $x = 200$ mm. Differential ablation or thermal expansion at this location could potentially create roughness that would trip the boundary layer. Thus, the model was designed with a 76.2-mm-long nosetip (38.1% of 200 mm) that can attach to the frustum forming backward- and forward-facing steps. The nosetip and the cover that allows access to the nosetip/frustum attachment are fabricated from 15-5 stainless steel. The frustum is 7075T6 aluminum.

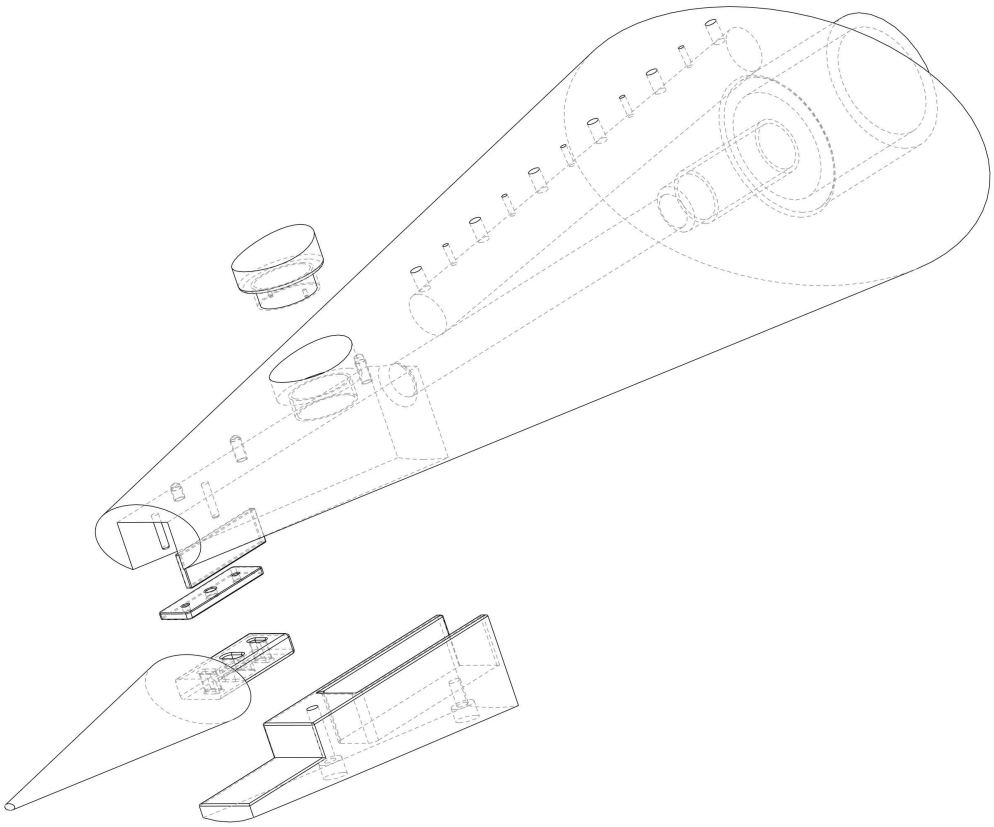

Figure 6: Exploded assembly drawing of HIFiRE-5 model

A glow perturber can be installed on the centerline at $x = 150$ mm. A blank plug made of 15-5 stainless steel occupies the 24-mm-diameter port in lieu of a perturber.

Eleven sensor holes are on the centerline starting at $x = 195$ mm. Their centers are evenly spaced in 12.5-mm increments (measured parallel to the model axis). The hole diameters alternate between 3.28 and 1.60 mm, starting with the larger diameter. The 3.28-mm-diameter holes are appropriate for 1/8-in.-diameter sensors such as PCB fast pressure sensors and Schmidt-Boelter heat transfer gages. The 1.60-mm-diameter holes fit 1/16-in.-diameter coaxial thermocouples and heat transfer gages. Dowel pins were used to plug the holes when sensors were not installed.

For most tests, three 1/8-in.- (3.2-mm-) diameter PCB model 132A31 pressure transducers were installed along the model centerline at $x = 220$, 270, and 320 mm and a 1/8 in.- (3.2-mm) diameter Medtherm 8-2FSB-0.25-36-20835 Schmidt-Boelter heat transfer gauge was installed at $x = 295$ mm. When using PCB and Schmidt-Boelter gauges, blanks were installed in the model before applying the temperature-sensitive paint. Care was taken to ensure the blanks were as flush as possible with the model surface. After the painting was finished, these blanks were carefully removed and the PCBs and Schmidt-Boelter were installed. The goal was then to install the sensors flush with the paint. The sensors were secured with nail polish, which

has been found to be a strong enough adhesive to keep the sensors in place, but easy enough (with careful application of acetone) to remove that the sensors are usually not damaged. The nail polish is also thick enough that it fills in the gap between the sensor and its surrounding sensor hole and paint, resulting in a smoother contour between the sensor and paint.

A Mitutoyo Surftest SJ-301 profilometer was used to measure the surface defect. Typical steps were 15–25 μm between the model and sensor surface, with a gap of 100 μm between the sensor side wall and its hole. The impact of these discrete roughnesses upon transition is not well understood. Attempted measurements of smooth(er)-wall transition using only coaxial thermocouples were unsuccessful.[34]

The PCB faces cannot be contoured, so there is some deviation from the true surface shape. The sensor holes are normal to the model surface, not the model axis. The HIFiRE-5 model is flat in the streamwise direction and has 56-, 68-, and 88-mm radii of curvature in the spanwise direction at these locations. At the farthest upstream sensor, the deviation between the model centerline contour and sensor face is a mere 0.02 mm, and the difference is less for the farther-aft sensors where the radius of curvature is less. This height is less than 1% of the boundary layer thickness predicted by CFD at this location (Section III). Thus, the effect of the sensors on the flow was neglected.

Many previous models studied with temperature-sensitive paint in the BAM6QT have been fabricated with nylon in the regions where TSP is applied, whereas the HIFiRE-5 model has an aluminum frustum. Nylon provides superior insulation, resulting in higher temperature change and a better signal-to-noise ratio. However, it is more difficult to calculate heat transfer for the nylon model than for a thin insulator on aluminum. Aluminum has several other advantages over nylon — it is more dimensionally stable for varying temperature, fewer mating parts need to be machined and assembled, thermocouples can more nearly match its thermal properties, etc. For these reasons, aluminum was chosen for the frustum.

VI. Temperature-Sensitive Paint (TSP) Instrumentation

A. Paint and Insulator

Three different airbrush insulators and a fourth spray-paint insulator were tested on the HIFiRE-5. The first insulator tested was Industrial Nanotech Inc. (INI) Nansulate Home Protect Interior thinned with tap water. The first two attempts to apply this insulator were frustrated by poor adherence to the model. Continued adjustments to the paint/thinner ratio resulted in an insulator that would stick, but was not very smooth. The texture resembled that of an orange peel, a common problem for airbrushed paints (Figure 7). This insulator proved to be the roughest surface finish tested. Not realizing its significance, a measurement of the finish with the group's Mitutoyo Surftest SJ-301 profilometer was not made. Photographs of the painted surface were taken through a microscope at 40× magnification (Figure 8). The left edge of the image is a ruler with lines engraved at 1/64 in. (0.397 mm) intervals. The bumps are spaced about 1 mm from one another and are roughly 0.2 mm high.

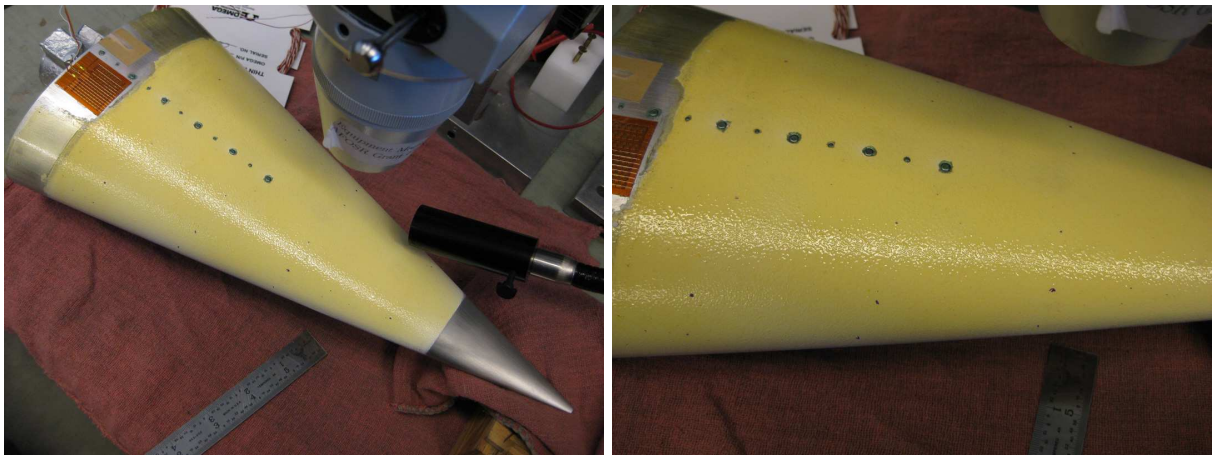

(a) (b)

Figure 7: Photographs of first TSP application showing 'orange-peel' roughness

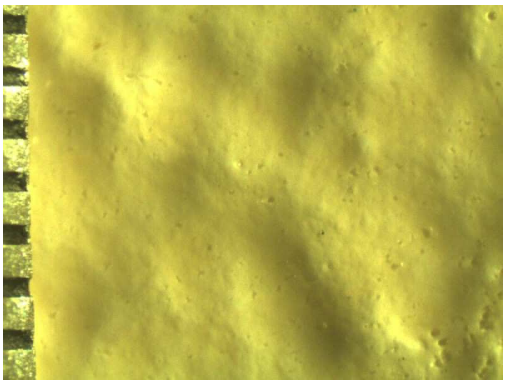

Figure 8: Photograph of orange peel paint finish through microscope at 40× magnification. Left side of image shows a ruler with 1/64-in. (0.397-mm) engravings. Individual bumps have ≈ 1-mm spacing.

The best insulator used was Top Flite LustreKote spray paint. Three coats of the white primer were followed by three or four coats of the jet white top coat. The spray paint is quicker and easier to apply than any airbrush formulation because no mixing is required beforehand and cleanup is trivial. Good uniformity is achieved after several even, thin coats (Figure 9). The thermal conductivity is not as low as the best insulator but much better than the worst.

(a) (b)

Figure 9: Photographs of final TSP application on spray-paint insulator

The TSP itself was a Ru(bpy) luminophore dissolved in ethanol and mixed into clear paint and applied by an airbrush. DuPont ClearCote was the original clear paint of choice, but it was discontinued by the manufacturer. BASF LIMCO LC4000 Clearcoat with LIMCO LHM hardener was selected as the replacement, but it seems to respond to pressure as well as temperature changes (see Reference 35 and below).

1. Paint Roughness and Thickness

The profilometer found root-mean-square surface finishes of 0.17–0.42 μm for the LustreKote. All TSP images reported herein except Figure 29b use this insulator. They all are regarded as having a 'smooth' finish.

The multiple layers of spray paint necessarily have some finite thickness. These layers consist of not only the TSP insulator but also several coats of the TSP itself. This thickness creates a forward-facing step at the front edge of the frustum. One option to mitigate this step is to paint the entire model, adding some

thickness to the entire surface. Perhaps this thickness would have some variation, but at least there would be no discontinuities. This approach was considered for the HIFiRE-5, but was rejected because of the uncertain effect it would have on the nosetip geometry. The nosetip was machined carefully to be a 0.381 scale match of the true shape, and applying paint to this sensitive region would have an unknown influence on the BAM6QT results.

Instead, the decision was made to paint only the aluminum frustum (and its inserts), leaving the steel nosetip unpainted. The thickness of the final TSP application (LustreKote spray paint plus TSP) was measured and found to be 0.33 mm (0.013 in.). Until the final session of TSP data collection, this forward-facing step existed at $x = 76.2$ mm. Before the final set of TSP data was gathered, fine-grit sandpaper was used to taper the upstream edge of the paint. The Mitutoyo profilometer was used to measure the step before and after sanding, but it proved to be ineffective for the steeper pre-sanded step.

Figure 10 shows profiles of the forward-facing step at the nosetip/frustum junction. The pre-sanding profile (dotted line) is an estimate based on the initial slope determined by the profilometer and the paint thickness measured by the gauge blocks. The after-sanding profile (solid line) is the profilometer measurement.

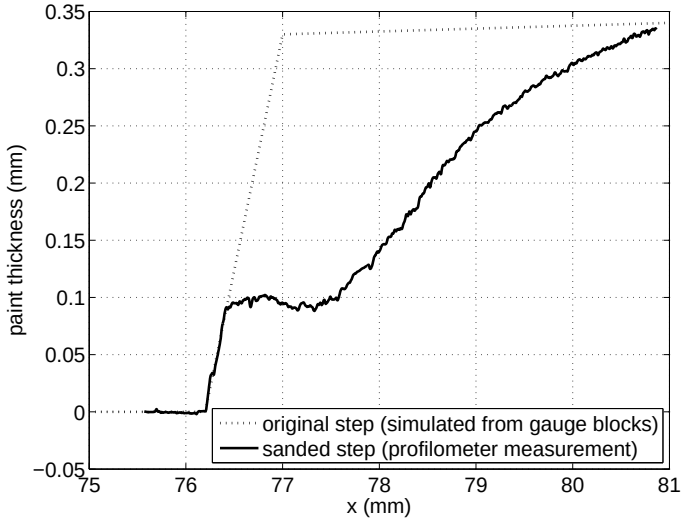

Figure 10: Profile of forward-facing step at nosetip/frustum junction. LustreKote spray paint plus TSP

Almost all TSP data presented in this report was collected with a relatively smooth paint finish. The only exception is Figure 29b, part of the assessment of the effect of surface finish on transition. Most of the 'smooth'-finish data was collected with the tapered step. The data from high-pressure runs (any images through the porthole windows) were collected with the unsanded paint edge. Except for Figures 31a (which illustrates the negligible effect of the step) and 29b, all TSP images through the large window are with the tapered paint edge. Table 1 summarizes the paint roughness for all the TSP data.

Table 1: Summary of paint roughness and step for TSP data

Figure	Surface Finish		Step
	Qualitative	Quantitative	
29b	orange peel	0.2-mm high lumps with 1-mm spacing	untapered
31a and all high-pressure ($p_0 > 1050$ kPa)	'smooth'	rms surface finish 0.17–0.42 μm	untapered
all others	'smooth'	rms surface finish 0.17–0.42 μm	tapered

B. Lights and Camera

The paint was excited by two blue (465 nm wavelength) light emitting diode (LED) arrays. The newer ISSI LM2xLZ-465 LED array has significantly more brightness, enabling shorter exposure times. Using the two lights in conjunction also provided more uniform illumination and reduced shadows from the window frame that would otherwise obscure portions of the model.

Ru(bpy) is excited by blue light and fluoresces orange. Thus, an orange filter (556 nm wavelength high-pass) was used to limit the incident light entering the camera, leaving only the fluoresced output.

A Cooke Corporation PCO.1200 14-bit CCD camera controlled by CamWare software was used. Its array is nominally 1600×1200 pixels, but 2×2 binning was selected, reducing the image size to 800×600 pixels. Binning reduces noise in the image and reduces the image size, allowing a faster frame rate with the limited transmission speed between camera and computer. Spatial resolution is reduced, but is still sufficient at 3.0 pixels per mm (0.33 mm per pixel) in streamwise and spanwise directions. When using the porthole window with the smaller field of view, the camera was moved closer and spatial resolution was 4.2 pixels per mm (0.24 mm per pixel).

Figure 11 is a photograph of the TSP hardware set up for the BAM6QT. The 7×14 in. (0.18×0.36 m) plexiglass window is installed in the north large window opening in the test section. The HIFiRE model is visible through the window. The camera (blue box) and one LED array (black cylinder) are in the foreground.

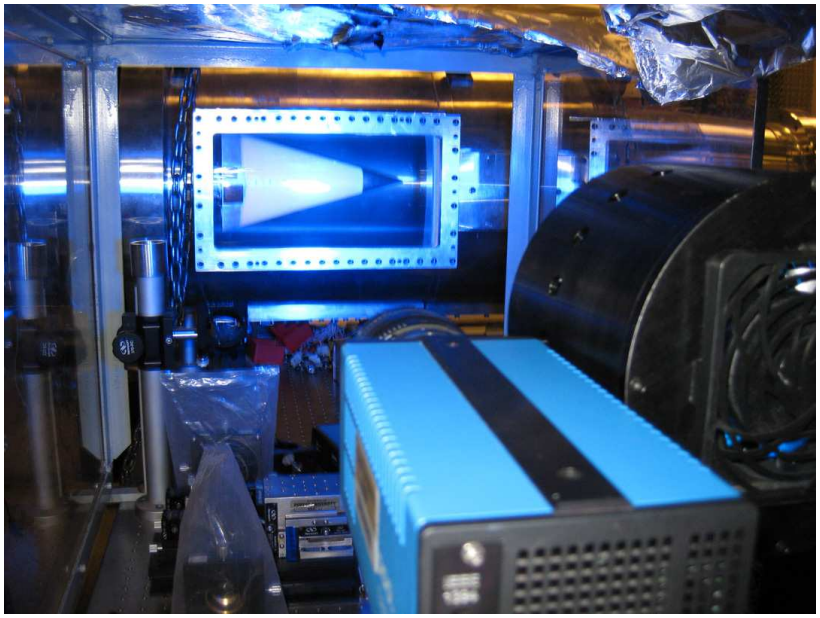

Figure 11: Camera and light source setup in the BAM6QT with HIFiRE-5 model visible through big window

The large rectangular window has the obvious benefit that the entire model is visible. However, it is limited to a maximum working pressure of 950 kPa (138 psi) gauge, or 1050 kPa (153 psi) absolute. In the terminology of the BAM6QT research group, runs at $p_0 > 1050$ kPa are regarded as 'high-pressure' because they require switching to porthole windows with a higher maximum allowable working pressure and using a boost pump to reach pressures in excess of the main air compressor's ≈ 1000 kPa output.[36] The TSP images from the several high-pressure runs conducted have a limited field of view circumscribed by a circular window frame.

The exposure time was varied from run to run to fill most of the CCD's bit depth. The most common exposure was 10 ms, but it sometimes varied within ± 2 ms. These changes in the settings are not expected to affect the output temperature as long as the settings were consistent for the dark, flow-off, and flow-on images (see below). The camera was set to record at 20 Hz (near the maximum data transfer rate), starting with the run start.

VII. Temperature-Sensitive Paint Data Analysis Methodology

A. TSP Calibration

Temperature sensitive paint intensity ratios are proportional to the temperature ratio between the two images.[37] For each run, a 'dark' image was recorded with the LED array off. A few seconds before the run, the LED array was turned on and an image was recorded with the flow 'off'. Then during the run, 'on' images were recorded. The contour plots display the temperature difference between the 'on' and 'off' images:

$$\Delta T = T_{\text{on}} - T_{\text{off}} = f\left(\frac{I_{\text{on}} - I_{\text{dark}}}{I_{\text{off}} - I_{\text{dark}}}\right) \tag{1}$$

A thermocouple attached to the base of the model typically indicated $T_{\text{off}} = 290$–320 K. It is surprising that $\Delta T < 0$ occasionally. It appears that some batches of TSP are sensitive to pressure as well as temperature. When each tunnel run began, the paint intensity changed in response to the large pressure drop from stagnation to static. The static pressure also varies during a run, but the change at startup is the larger effect. Rubal found that a +2–3 K correction to BAM6QT TSP data is in order (that is, if the TSP indicates $\Delta T = 1$ K, the true ΔT on which to base heat-flux computation is 3–4 K).[38] Because the proper means of reducing TSP contours to heat flux has yet to be determined with confidence, uncorrected ΔT is presented herein.

The TSP calibration was based on Figure 3.13 'Temperature dependencies of the luminescence intensity for TSP' from Reference 37. A linear fit to the I/I_{ref} vs. T curve for Ru(bpy) between 15 and 60 °C (288–333 K) was computed. This approximation has the benefit of a simple implementation and is accurate over the temperature range encountered. The resulting calibration equation is:

$$\Delta T = (362 - T_{\text{ref}}) \cdot \left(1 - \left(\frac{I_{\text{on}} - I_{\text{dark}}}{I_{\text{off}} - I_{\text{dark}}}\right)\right) \tag{2}$$

where T_{ref} is the wind-off (or pre-run) model temperature measured by the thermocouple on the model base with units of Kelvin. When the pre-run model temperature was unavailable, 310 K was used as an estimate because it is in the middle of the typical range. The scale of the temperature contour for each figure was adjusted to maximize the detail both before and after transition.

B. Transition Threshold

Transition onset was inferred from a temperature rise along the centerline. The centerline profiles presented later were used in conjunction with the overall temperature contour plots. There was typically some variation in the temperature profile, so a simple search for the minimum temperature was not sufficient. The temperature rise at higher freestream Reynolds number tended to be steeper, whereas at low Re the rise might be very gradual with a greater uncertainty in transition location.

Figure 12 presents a typical noisy-flow TSP contour plot as well as the temperature profile along the centerline extracted from the global contour. The centerline trace enables greater precision in finding streamwise location, but the TSP images are essential to identifying the effects of unpainted sensors and sensor blanks, registration marks, window frame shadows, and any other stray influences. To reduce noise in the data, the paint intensity was averaged within 3.5 mm (12 pixels) of the centerline. This width was chosen so that only the data between the off-centerline hot streaks were included. These spanwise strips were then smoothed further with a streamwise 3-pixel moving average (±0.33-mm for the big window, 0.25-mm for the smaller field-of-view porthole). Gaps in the profiles exist where the data from the sensor locations (centered at $x = 220$, 270, 295, and 320 mm) were excised. The temperature along the centerline starts increasing at $x \approx 145$ mm, so this location is reported for the onset of transition. Note that due to the limits inherent in contour plots, the temperature rise is not apparent in the contour until the temperature has risen by ≈ 0.4 K at $x = 165$ mm.

Under noisy flow, it is estimated that the transition location is accurate within less than 10% — roughly 150 ± 10 mm at higher Re and 250 ± 20 mm at lower Re. The percent error in transition location is slightly reduced under quiet flow because the uncertainty is proportional to Re. Therefore the uncertainty under quiet flow was similarly ±10 mm, but relative to a larger value of approximately 250 mm, or less than 5%.

Identifying the onset of crossflow transition is somewhat more difficult, especially under quiet flow. The crossflow transition front is not a straight line perpendicular to the centerline, so a single number would not

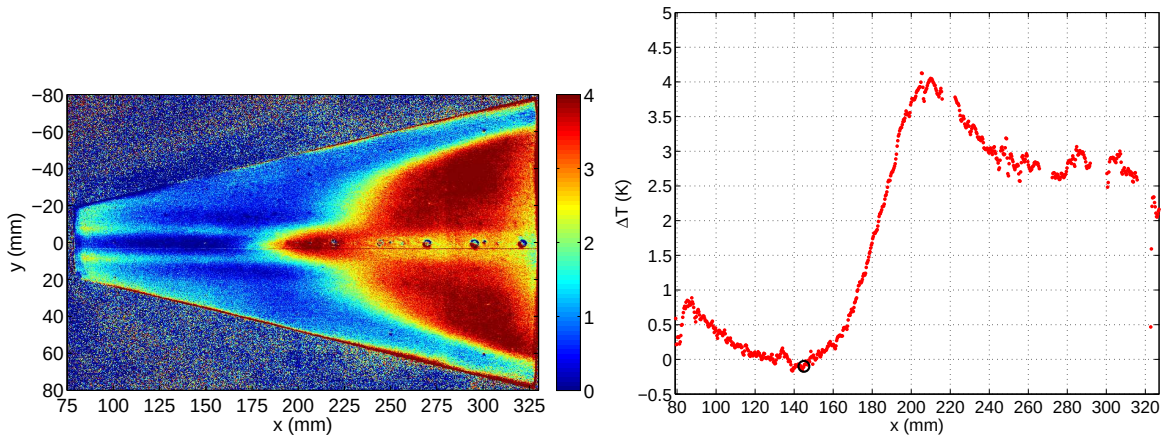

(a) ΔT (K)

(b) Centerline profile. Black circle marks inferred transition onset

Figure 12: Representative TSP contour and centerline profile. Noisy flow, $M = 5.8$, $\alpha = 4°$, $Re = 8.1 \cdot 10^6$ /m, $p_0 = 610$ kPa

fully characterize its location. As will be seen, under quiet flow numerous streamwise hot streaks are evident over a long distance. Eventually their temperature increases more rapidly, but it does not reach a minimum beforehand. Whereas amplifying second-mode waves would not be expected to significantly impact heating, crossflow vortices would influence heating by virtue of their effect upon the boundary layer thickness even prior to their breakdown to turbulence due to secondary instabilities. Thus the effect of crossflow can be qualitatively perceived by TSP, but a quantitative determination of the location of crossflow transition is not made.

VIII. Temperature-Sensitive Paint Results and Discussion

A. Effect of Noise Level

Figure 13 illustrates the effect of tunnel noise level on the HIFiRE-5 at $\alpha = 0°$ and $Re = 10.2 \cdot 10^6$ /m. Transition onset on the centerline is delayed from $x = 130$ mm under noisy flow to $x = 270$ mm under quiet flow. The streamwise profiles used to judge transition location are contained in Figures 22 and 24. Centerline transition is presumed to be due to the amplification and breakdown of second-mode waves. Crossflow is absent on the centerline because it is an axis of symmetry without a spanwise velocity component. Computations predict a Mach number at the boundary layer edge of about 5 for this case (see Section III); second-mode waves are more amplified than first-mode for an edge Mach number this large and a cold model wall ($T_{\text{wall}} \approx 0.7T_0$).[39] Furthermore, disturbance frequencies measured along the centerline match computational predictions of second-mode frequencies more closely than first mode.[25]

Under noisy flow, transition appears to initiate off the centerline as well as on it, resulting in a three-lobed transition front. This transition away from the centerline is presumed to arise from the amplification and breakdown of crossflow vortices. Under quiet flow at this Re, it is not clear whether the onset of crossflow transition has begun. Streamwise streaks of elevated heating are visible. It is suspected that these streaks are due to crossflow vortices that have not yet broken down to turbulence. They are roughly aligned with the inviscid streamlines. The streaks do not broaden into a turbulent wedge, but instead remain distinct to the back end of the model. It is anticipated that a secondary instability would ultimately lead to breakdown of the stationary crossflow vortices into turbulence, but this process was not observed even at the highest Re achievable under quiet flow. Perhaps the low tunnel noise has reduced the amplitude of the traveling secondary instability. There is no local maximum of heating that would indicate a fully-turbulent boundary layer. It is difficult to determine the location of transition onset or fully-turbulent flow.

Unlike the second-mode waves, which are traveling waves, stationary crossflow vortices under quiet flow are detected by TSP, which is monotonic in the mean heat transfer. Although crossflow-induced transition is evident under noisy flow, individual streaks are only visible under quiet flow. This difference may arise

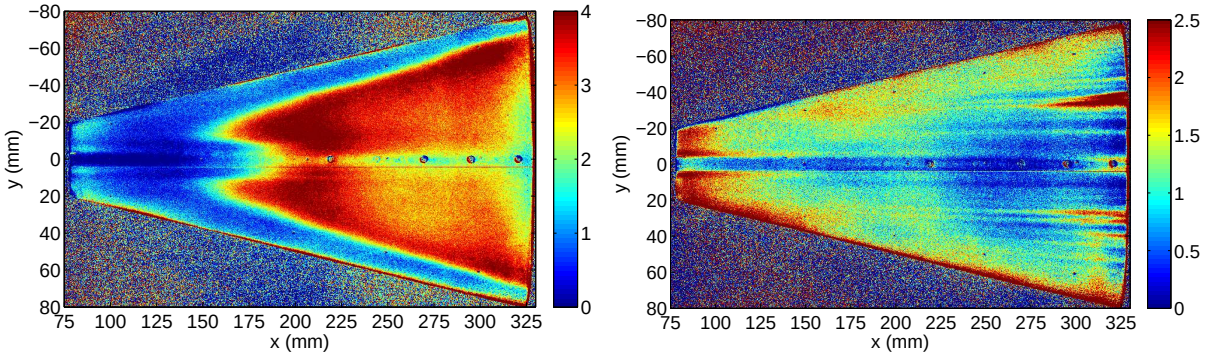

(a) Noisy flow, $M = 5.8$, $p_0 = 810$ kPa, $T_0 = 410$ K, $t = 4.5$ s (b) Quiet flow, $M = 6.0$, $p_0 = 940$ kPa, $T_0 = 429$ K, $t = 0.5$ s

Figure 13: Effect of tunnel noise level. $\alpha = 0°$, $Re = 10.2 \cdot 10^6$ /m

from the relative stability of traveling and stationary crossflow vortices. References 40 and 41 explain that stationary waves are dominant in low-noise environments, at least at low speeds.

The centerline transition result is significant because it is the first evidence in the BAM6QT of transition under quiet flow that is not induced by deliberately-generated roughness. Until now, quiet-flow transition had been detected only on vehicles with isolated roughness elements intended to trip the boundary layer, such as the X-51[42,43] and HIFiRE-1.[5] Conclusions regarding the effect of noise level on (relatively) smooth walls had been limited to setting a lower bound on the delay.

A noise level comparison at a higher freestream Reynolds number shows the same effect of tunnel noise, but more features are visible in the model boundary layer under (nominally) quiet flow (Figure 14). Centerline transition is delayed from $x = 125$ to 255 mm. Crossflow transition is evident under noisy flow; hot streaks thought to arise from crossflow vortices and possible transition from these vortices exists under quiet flow, but further from the nose. At the time these data were collected, the maximum useful quiet pressure of the BAM6QT was 1170 kPa (169 psia).[44] As discussed above in Section IV, low noise levels at this high pressure this far back in the nozzle have not been proven.

Tests at these high pressures necessitate use of the porthole windows, which restrict the field of view (see Section VI). Note that the noisy-flow image is viewing the front half of the frustum, roughly the middle third of the model, whereas the range of the image under quiet flow is the aft third. The model was repositioned between tunnel runs so that the transition front was visible through the downstream porthole window. The TSP contour plots for images through the porthole windows are shown on the same axes as the images through the big window. This presentation makes the relative locations of the images easier to see.

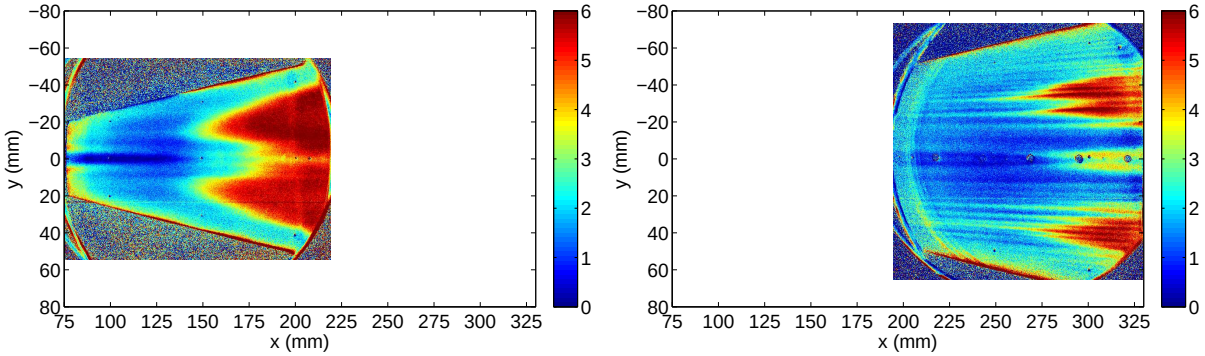

(a) Noisy flow, $M = 5.8$, $p_0 = 930$ kPa, $T_0 = 408$ K, $t = 5.0$ s (b) Quiet flow, $M = 6.0$, $p_0 = 1090$ kPa, $T_0 = 429$ K, $t = 0.5$ s

Figure 14: Effect of tunnel noise level at high pressure. $\alpha = 0°$, $Re = 11.8 \cdot 10^6$ /m

Figure 15 shows a spanwise temperature profile for the contour plot shown in Figure 14b at $x = 255$ and 305 mm. This case (maximum quiet pressure, $\alpha = 0°$) is particularly interesting because it exhibits the maximum impact of crossflow encountered. The upstream location coincides with the apparent onset of

transition along the centerline. The data was averaged over ±2 mm (8 pixels) in the streamwise direction and ±0.24 mm (1 pixel) in the spanwise direction.

The centerline and off-centerline temperature increases are visible. The hot streaks thought to arise from crossflow vortices persist into the region of presumed turbulent or transitional flow. These streaks are spaced about 3.0 mm from one another at $x = 305$ mm and they are inclined 4–5° away from the centerline. As discussed previously, it is unclear what is an appropriate threshold for transition onset or end for crossflow transition, especially under quiet flow.

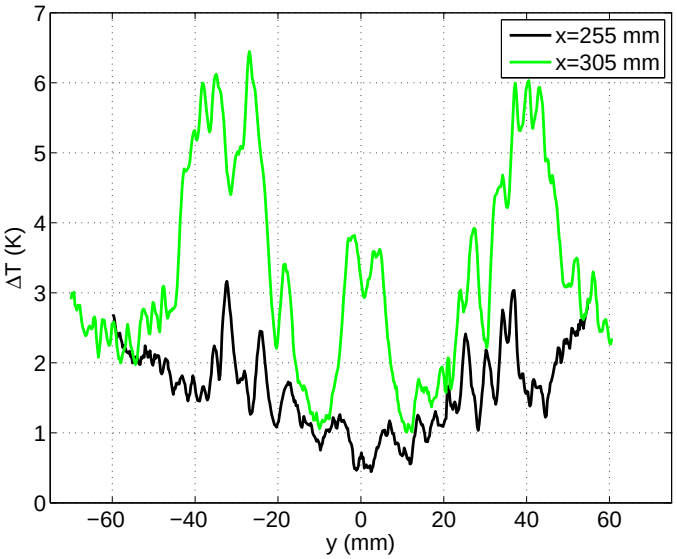

Figure 15: Spanwise temperature profile. Quiet flow, $M = 6.0$, $\alpha = 0°$, $Re = 11.8 \cdot 10^6$ /m, $p_0 = 1090$ kPa

Figure 16 shows a noise comparison for $\alpha = 4°$ on the windward side at $Re = 9.5 \cdot 10^6$ /m. The significant effect of noise level on transition is again obvious. Under noisy flow, both second-mode- and crossflow-induced transition appear to occur. Transition onset due to second-mode waves begins on the centerline at approximately $x = 140$ mm for these conditions. Crossflow transition begins at roughly 180 mm, but it is again difficult to set a threshold. Upstream of $x = 140$ mm, the temperature contours are very similar for both noise levels.

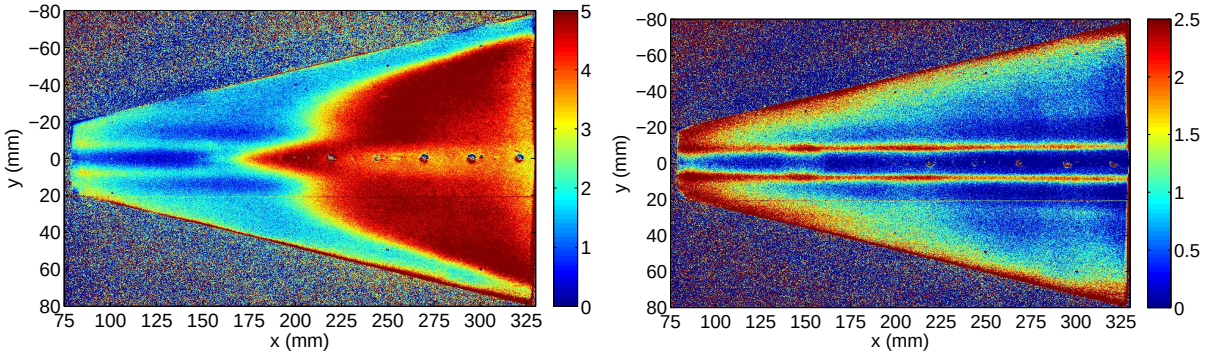

(a) Noisy flow, $M = 5.8$, $p_0 = 720$ kPa, $T_0 = 397$ K, $t = 7.5$ s (b) Quiet flow, $M = 6.0$, $p_0 = 810$ kPa, $T_0 = 410$ K, $t = 2.8$ s

Figure 16: Effect of tunnel noise level. $\alpha = 4°$, $Re = 9.5 \cdot 10^6$ /m

Under quiet flow, on the other hand, transition does not occur as a result of either instability. Two hot streaks parallel with the centerline run the entire length of the painted portion of the model. The streaks are approximately 4 mm wide and centered 9 mm from the centerline. The temperature between these streaks is lower than elsewhere on the surface. The explanation for this temperature distribution is not obvious from the TSP data, but the CFD simulations and Princeton Filtered Rayleigh Scattering experiments are

helpful. They both show a thicker boundary layer along the centerline, which would result in lower heat flux. Vortices form on each side of the centerline bulge, which cause the boundary layer to be thinner and would appear as a higher temperature.

Figure 17 illustrates a similar noise effect as Figure 16, except at p_0 near the tunnel's maximum quiet pressure. Note that the horizontal scales for these two subfigures differ because, as with Figure 14, the model was repositioned between runs so different portions were visible through the porthole windows. The most significant difference observed at this higher Re is the evidence of centerline transition under quiet flow. Transition onset occurs at $x \approx 275$ mm under quiet flow in Figure 17b. Unlike the hot streaks on either side of centerline, the elevated centerline heating widens downstream in the classic turbulent wedge. The apparently higher and wider heating at the tip of the centerline transition under noisy flow is an artifact arising from the steel insert for the glow perturber, which is centered at $x = 150$ mm.

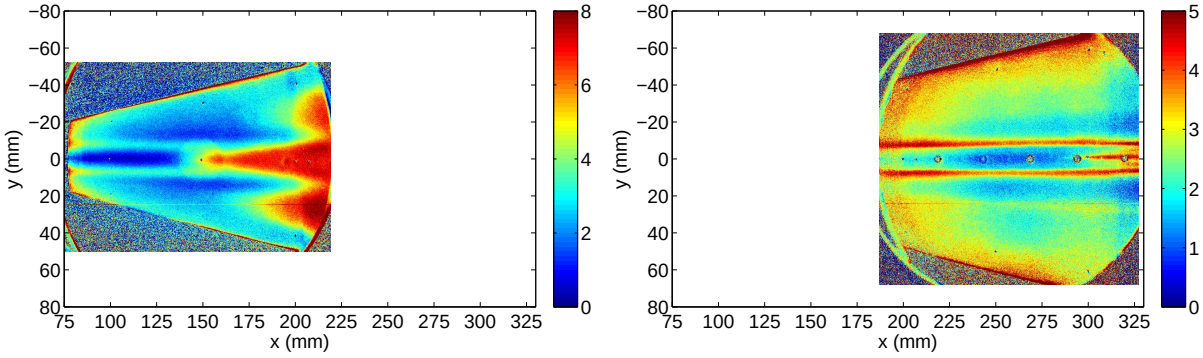

(a) Noisy flow, $M = 5.8$, $p_0 = 950$ kPa, $T_0 = 410$ K, $t = 4.5$ s (b) Quiet flow, $M = 6.0$, $p_0 = 1100$ kPa, $T_0 = 428$ K, $t = 0.5$ s

Figure 17: Effect of tunnel noise level at high pressure. $\alpha = 4°$, $Re = 11.9 \cdot 10^6$ /m

B. Effect of Angle of Attack

Tests were run at 0 and 4° (windward side) angle of attack. Figure 18 shows the TSP result from two runs at $Re \approx 11.8 \cdot 10^6$ /m under quiet flow. The most striking difference due to angle of attack is that the streaks suspected to arise from crossflow vortices at $\alpha = 0$ are entirely absent at $\alpha = 4°$. This observation can be explained by the altered pressure gradient when α changes. On the windward face, as angle of attack increases, the centerline static pressure increases relative to the leading edge pressure, thereby weakening the pressure gradient that creates crossflow vortices and causes ballooning of the centerline boundary layer. This trend is the opposite of what is encountered when studying crossflow on circular cones, for which increasing angle of attack corresponds to increasing crossflow. Centerline transition is delayed from $x = 255$ mm for $\alpha = 0°$ to $x = 275$ mm for $\alpha = 4°$. The centerline temperature profiles used to gauge transition location appear below.

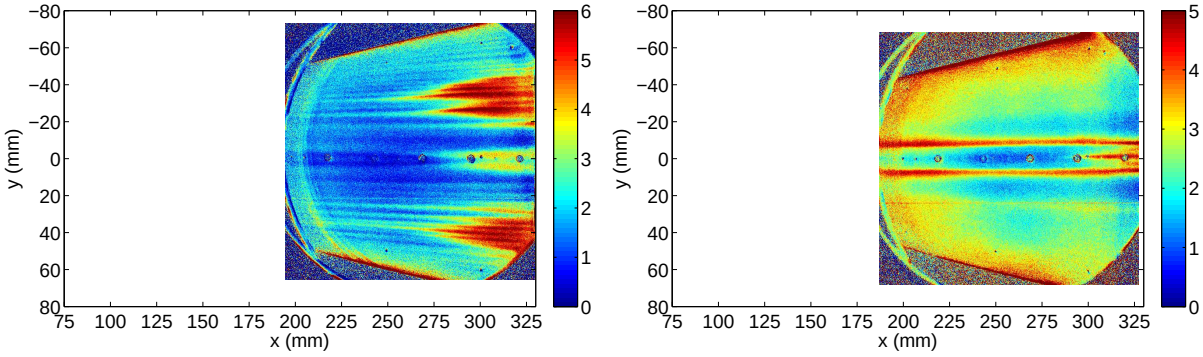

(a) $\alpha = 0°$, $Re = 11.8 \cdot 10^6$ /m, $p_0 = 1090$ kPa (b) $\alpha = 4°$, $Re = 11.9 \cdot 10^6$ /m, $p_0 = 1100$ kPa

Figure 18: Effect of angle of attack. Quiet flow, $M = 6.0$, $t = 0.5$ s

Figure 19 shows the spanwise temperature profiles at $x = 305$ mm for the two images in Figure 18. It was constructed the same as Figure 15 — the data was averaged over ±2 mm (8 pixels) in the streamwise direction and ±0.24 mm (1 pixel) in the spanwise direction. Both angles of attack demonstrated elevated heating along the centerline at this location, suggesting that the boundary layer is transitional or turbulent. The narrow off-centerline hot streaks stand out clearly for $\alpha = 4°$ at $y = \pm 8$ mm. The temperature for $y = 20$–50 mm on both sides of the centerline is much higher for $\alpha = 0°$, which agrees with the observation that crossflow transition has begun only for this angle of attack.

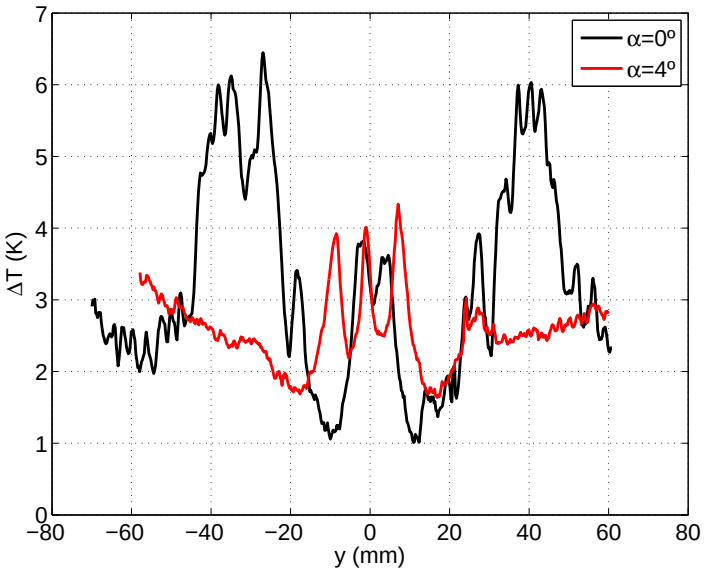

Figure 19: Effect of angle of attack on spanwise temperature profile. Quiet flow, $M = 6.0$, $x = 305$ mm

Similar trends were observed when varying angle of attack under noisy flow, as seen in Figure 20. As under quiet flow, crossflow transition is delayed under noisy flow at higher angle of attack. The centerline transition delay is again much smaller, from $x = 130$ to 140 mm.

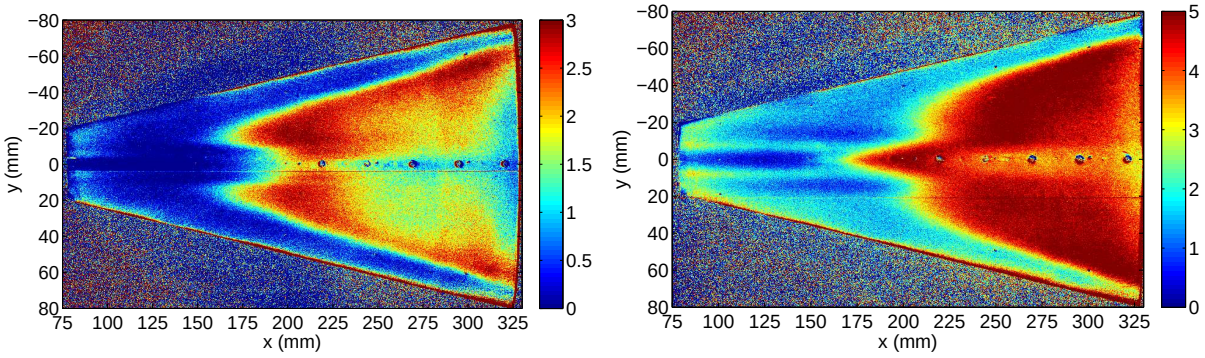

(a) $\alpha = 0°$, $p_0 = 710$ kPa, $t = 7.95$ s

(b) $\alpha = 4°$, $p_0 = 720$ kPa, $t = 7.5$ s

Figure 20: Effect of angle of attack. Noisy flow, $M = 5.8$, $Re = 9.5 \cdot 10^6$ /m

Regardless of noise level, both angles of attack show low temperatures near the centerline prior to transition. For $\alpha = 4°$, the low-temperature region is wider and bordered by hot streaks. For both quiet and conventional noise levels, the overall temperatures are higher at higher angle of attack, which is attributed to the thinner boundary layer on the windward side.

C. Effect of Freestream Reynolds Number at Zero Angle of Attack

Figure 21 illustrates the effect of freestream Re on transition under quiet flow for $\alpha = 0$. The scale of the temperature contours was adjusted for each subfigure to make flow features more perceptible at the expense of a direct temperature comparison. For all cases, heating is lower on the centerline and highest near the leading edges. Off-centerline heating decreases as the boundary layer thickens downstream. No transition is present for the three lower-Re cases shown. Centerline transition onset is detected at $x = 270$ mm for $Re = 10.2 \cdot 10^6$ /m or Re_x of $2.8 \cdot 10^6$. For the highest Re shown, $11.8 \cdot 10^6$ /m, transition on the centerline begins at $x \approx 255$ mm. This location corresponds to $Re_x = 3.0 \cdot 10^6$. As discussed previously, it cannot be stated with complete confidence that flow is completely quiet throughout the nozzle at these high Re. Thus, the quiet-flow transition locations are in fact the transition locations where the flow is presumed to still be quiet.

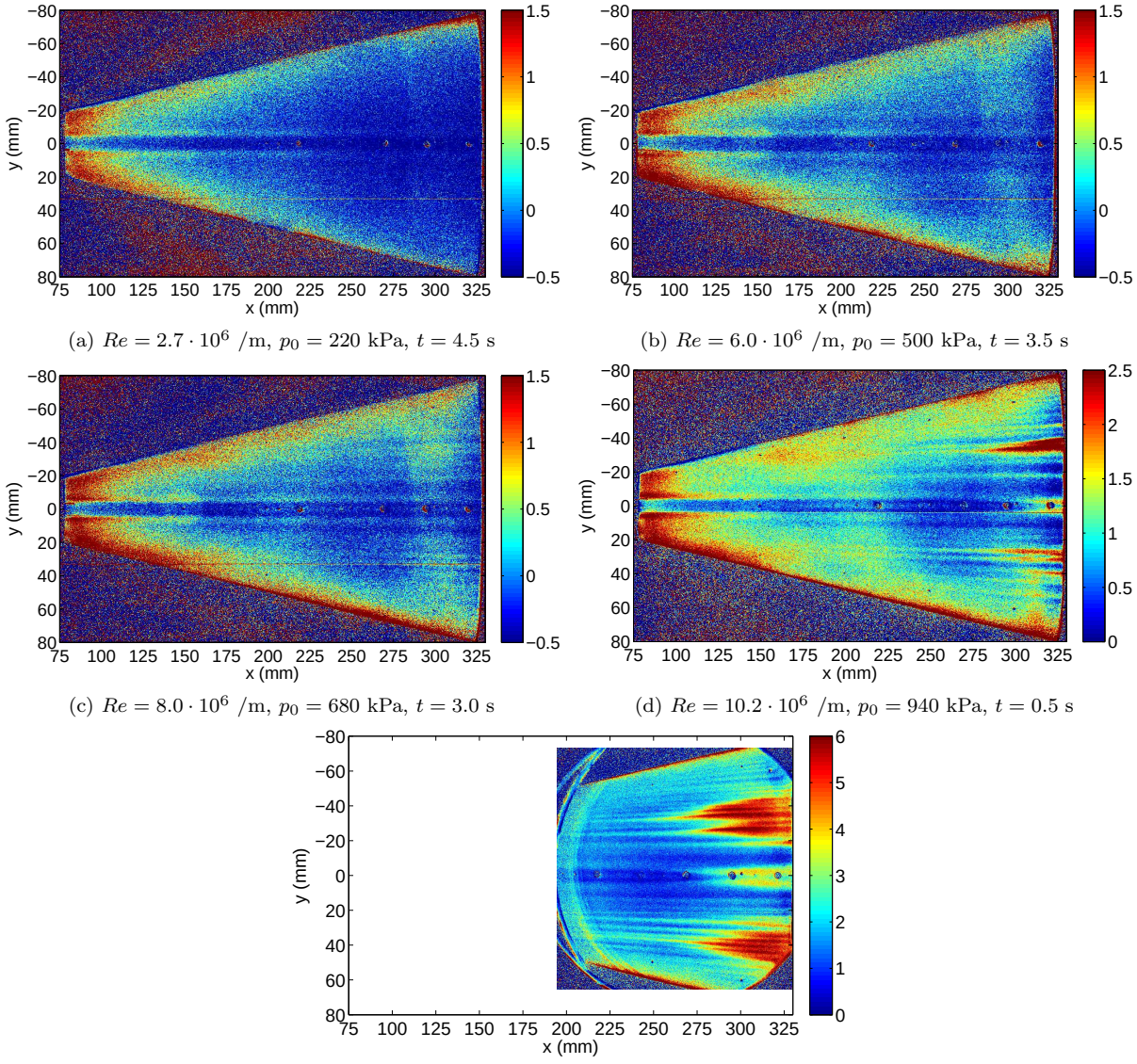

(a) $Re = 2.7 \cdot 10^6$ /m, $p_0 = 220$ kPa, $t = 4.5$ s

(b) $Re = 6.0 \cdot 10^6$ /m, $p_0 = 500$ kPa, $t = 3.5$ s

(c) $Re = 8.0 \cdot 10^6$ /m, $p_0 = 680$ kPa, $t = 3.0$ s

(d) $Re = 10.2 \cdot 10^6$ /m, $p_0 = 940$ kPa, $t = 0.5$ s

(e) $Re = 11.8 \cdot 10^6$ /m, $p_0 = 1090$ kPa, $t = 0.5$ s

Figure 21: Effect of varying freestream Re. Quiet flow, $M = 6.0$, $\alpha = 0°$

The temperature contours indicate higher T for the $Re = 6.0$ and $8.0 \cdot 10^6$ /m cases for approximately $285 < x < 315$ mm. These images are taken from later during their runs, after the nozzle-wall boundary layer has separated and reattached. These regions experienced higher heating under a turbulent model boundary layer during the period of separated flow and the TSP still exhibits the residual heating.

Streaks due to crossflow vortices are barely visible at $Re = 8.0 \cdot 10^6$ /m and become more obvious at higher Re. More streaks appear at the highest Re and they appear farther upstream. It is not clear whether the boundary layer transitions to turbulent before the end of the model as a result of these streaks or if the higher temperatures are due to increased laminar heating. The temperature increase is consistent with a transitional or turbulent boundary layer, but the streaks remain distinct, suggesting that the vortices have not broken down completely.

Figure 22 shows the centerline temperature rise for the five images in Figure 21. The centerline temperature rise was averaged within 3.5 mm (12 pixels) of the centerline. This width was chosen so that only the data between the off-centerline hot streaks were included. The data were then smoothed in the streamwise direction with a 3-pixel moving average (±0.33-mm for the big window, 0.25-mm for the smaller field-of-view porthole). Gaps in the profiles exist where the data from the sensor locations (centered at $x = 220$, 270, 295, and 320 mm) were excised. Narrow spikes occasionally appear at the registration mark locations ($x = 100$, 150, 200, 250, and 300 mm).

Figure 22 was used in conjunction with the whole-surface images to judge transition locations, which were determined as described above. They are marked with black circles and are summarized below in Table 2 after noisy-flow results are presented.

Naturally, there is some scatter and random variation in the temperature profile. For the three lower freestream unit Reynolds numbers (2.7, 6.0, and $8.0 \cdot 10^6$ /m), the temperature is mostly decreasing over the entire model length. It is thus concluded that the centerline transition does not occur in these cases. For $Re = 10.2 \cdot 10^6$ /m, ΔT begins to rise downstream of the sensor at $x = 270$ mm. The effect of the sensors on the surface contour was described in Chapter V. It is possible that the sensor affected transition in this or other cases, but its impact is unknown. Attempts to measure smoother-wall transition with coaxial thermocouples were unsuccessful. Transition onset occurs at $x = 255$ mm for the $Re = 11.8 \cdot 10^6$ /m case. The temperature reaches a maximum at $x = 310$ mm, which is assumed to coincide with the beginning of fully-turbulent flow. The transitional region in this case is 55-mm in length.

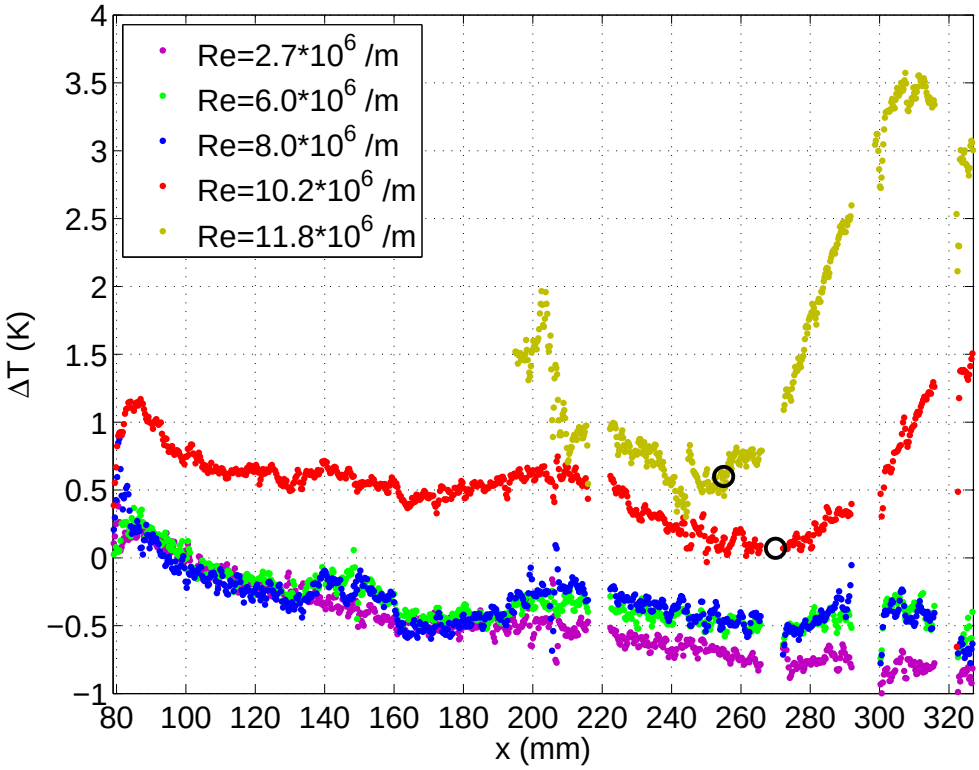

Figure 22: Centerline temperatures for $\alpha = 0°$ under quiet flow

Figure 23 contains TSP images at a range of freestream Reynolds numbers under noisy flow at $\alpha = 0$. It is uncertain whether second-mode and crossflow transition occur independently or crossflow transition

propagates to the centerline. As in Figure 21, the scale was varied to enhance detail at the expense of an easier temperature comparison. The signal-to-noise ratio is particularly poor for the $Re = 2.8 \cdot 10^6$ /m case, but the temperature does indeed increase starting near $x = 270$ mm. As expected, transition onset occurs farther forward as Re increases. The shape of the transition front is essentially the same for all Re, which suggests that the two transition modes are affected more or less equally by changing Re.

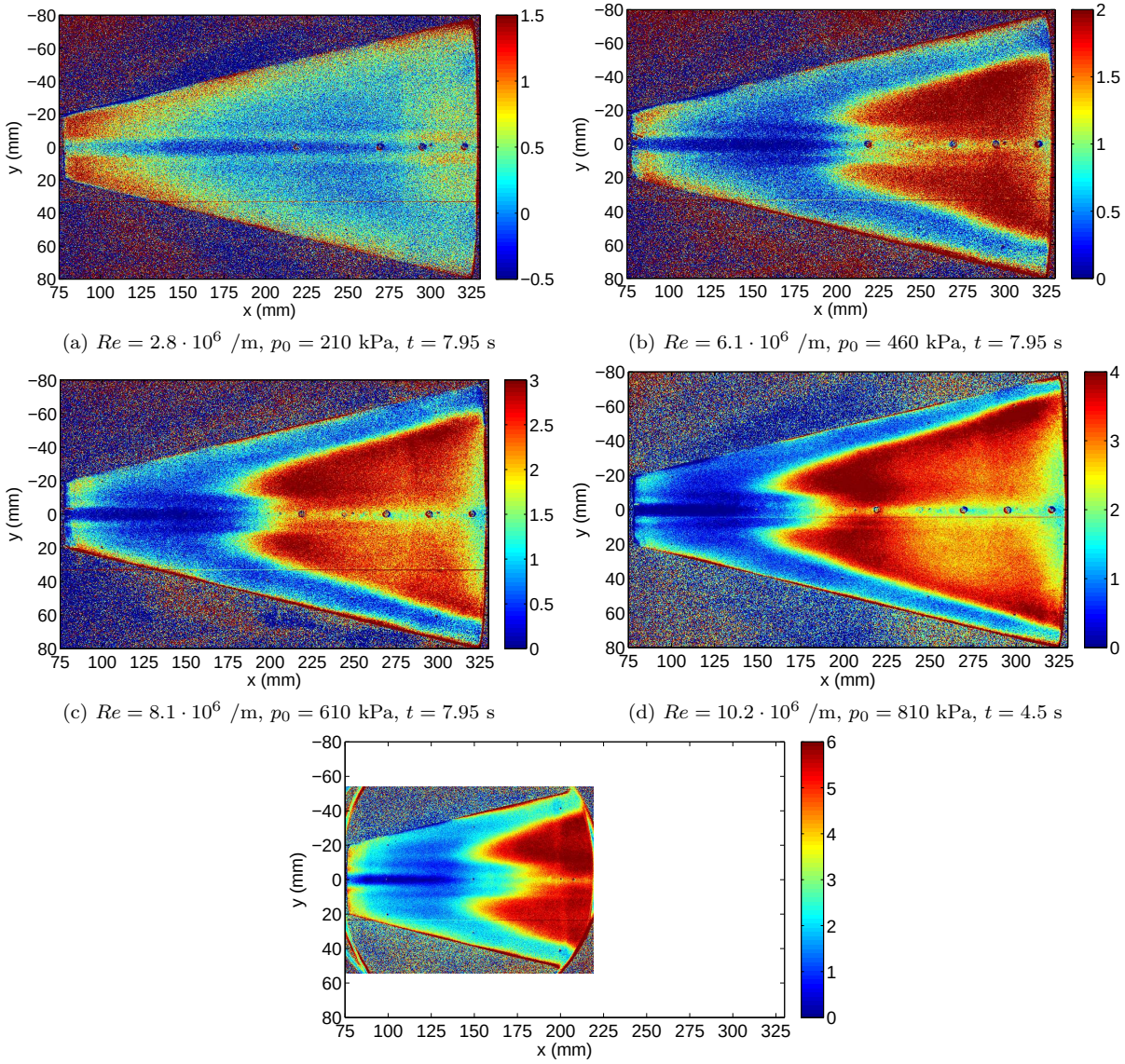

(a) $Re = 2.8 \cdot 10^6$ /m, $p_0 = 210$ kPa, $t = 7.95$ s

(b) $Re = 6.1 \cdot 10^6$ /m, $p_0 = 460$ kPa, $t = 7.95$ s

(c) $Re = 8.1 \cdot 10^6$ /m, $p_0 = 610$ kPa, $t = 7.95$ s

(d) $Re = 10.2 \cdot 10^6$ /m, $p_0 = 810$ kPa, $t = 4.5$ s

(e) $Re = 11.8 \cdot 10^6$ /m, $p_0 = 930$ kPa, $t = 5.0$ s

Figure 23: Effect of varying freestream Re. Noisy flow, $M = 5.8$, $\alpha = 0°$

Figure 24 shows the centerline temperature distribution for the $\alpha = 0°$ noisy-flow results gleaned from the images in Figure 23. It was constructed the same way as Figure 22. Unlike under quiet flow, centerline transition appears before the end of the model at all Re tested. The expected trend of earlier transition as Re increases is evident. Little importance should be given to the actual ΔT values reported because of the pressure dependence discussed previously.

Table 2 presents the transition locations measured with TSP for $\alpha = 0°$ under quiet and noisy flow. The freestream Reynolds numbers were matched as closely as possible when choosing the images to present, but it was not possible to match conditions within $0.1 \cdot 10^6$ /m for the low-Re quiet cases. Images early in the run were contaminated by nozzle-wall boundary-layer separation or other flow-quality problems, so images at later times were used (generally after reattachment at $t = 3$–5 s). Noisy-flow runs did not achieve these

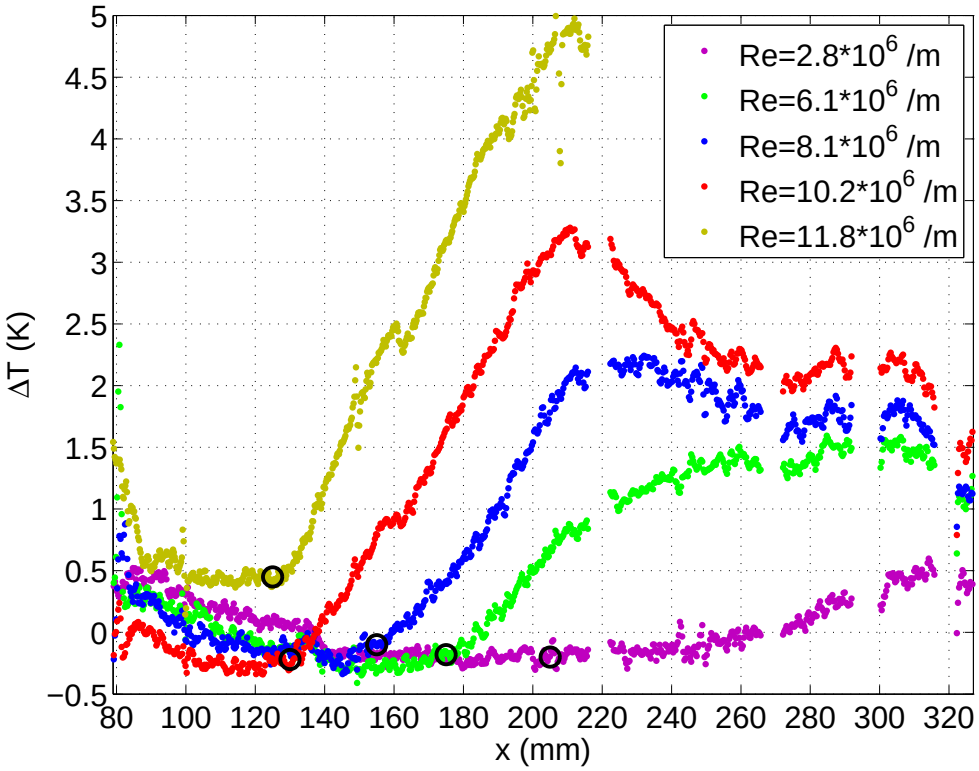

Figure 24: Centerline temperatures for $\alpha = 0°$ under noisy flow

lower Re until after data collection had ended, so the latest (lowest-Re) image is used for comparison. The difference in Re is only $0.1 \cdot 10^6$ /m, a 1–4% discrepancy.

The transition delay shown in the final column is the ratio between transition Re_x under quiet and noisy flow. It is unclear if Re_x is a proper scaling for transition location for this geometry, but these values at least give a rough assessment of the significant impact of tunnel noise on transition. Because transition is not observed for the three lower-Re cases shown, only a lower bound on the transition delay can be stated for them. It bears repeating that the higher-Re cases are significant because they are the first evidence in the BAM6QT of transition under quiet flow not induced by deliberately-generated roughness. In other words, the actual ratio between transition Re_x can be stated, rather than just a lower bound. However, once again it is warned that the quiet-flow transition results may have been contaminated by higher-than-quiet noise levels at the end of the test section. Even if the flow along the tunnel centerline was quiet, disturbances may propagate through the model boundary layer to affect transition.

Table 2: Summary of centerline transition locations for $\alpha = 0°$

Re	Location (mm)		Transition Re_x ($\cdot 10^6$)		Transition Delay
($\cdot 10^6$ /m)	Quiet	Noisy	Quiet	Noisy	quiet Re_x/ noisy Re_x
2.7–2.8	> 328	205	> 0.89	0.57	> 1.6
6.0–6.1	> 328	175	> 2.0	1.1	> 1.8
8.0–8.1	> 328	155	> 2.6	1.3	> 2.0
10.2	270	130	2.8	1.3	2.1
11.8	255	125	3.0	1.5	2.0

D. Effect of Freestream Reynolds Number at 4° Angle of Attack

Figure 25 illustrates the effect of freestream Re on transition under quiet flow for $\alpha = 4$. The boundary layer appears to be laminar over the entire model except for the highest Re tested, $11.9 \cdot 10^6$ /m, for which centerline transition occurs. There is no evidence of crossflow transition (or even crossflow vortices) at any Re tested. The relatively low-temperature centerline occurs as it did for $\alpha = 0°$. The distinct off-centerline hot streaks are not clear at the lowest Re shown ($2.6 \cdot 10^6$ /m), but are evident at all higher Re. At Re between the formation of the hot streaks and transition onset, there is very little change observed in the overall temperature distribution.

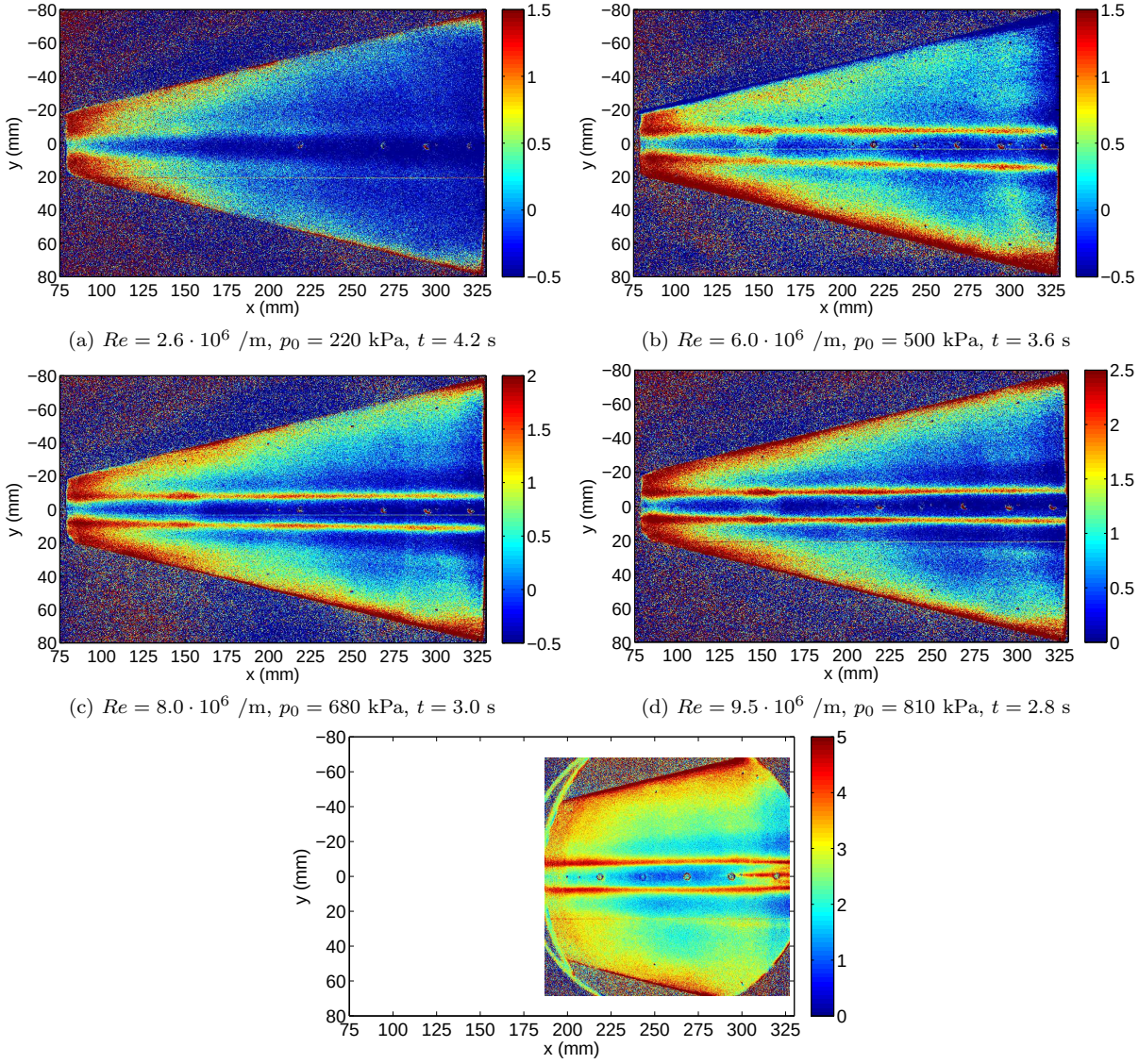

(a) $Re = 2.6 \cdot 10^6$ /m, $p_0 = 220$ kPa, $t = 4.2$ s

(b) $Re = 6.0 \cdot 10^6$ /m, $p_0 = 500$ kPa, $t = 3.6$ s

(c) $Re = 8.0 \cdot 10^6$ /m, $p_0 = 680$ kPa, $t = 3.0$ s

(d) $Re = 9.5 \cdot 10^6$ /m, $p_0 = 810$ kPa, $t = 2.8$ s

(e) $Re = 11.9 \cdot 10^6$ /m, $p_0 = 1100$ kPa, $t = 0.5$ s

Figure 25: Effect of varying freestream Re. Quiet flow, $M = 6.0$, $\alpha = 4°$

Figure 26 shows the centerline TSP intensity ratios for the five images in Figure 25. As with the other streamwise profiles, the paint intensity was averaged within 3.5 mm (12 pixels) of the centerline and then the spanwise strips were smoothed further with a 1-mm (3-pixel) moving average. Figure 26 corroborates the conclusion drawn from analyzing the TSP contour plots: the boundary layer is laminar for all cases except the highest. For $Re = 11.9 \cdot 10^6$ /m, centerline transition begins at $x = 275$ mm. The higher temperatures for $x = 180$–200 mm arise from reflections from the window frame.

The elevated temperature at $x = 150 \pm 12$ mm in Figure 26 is due to the steel glow perturber insert.

These images were all collected after the nozzle-wall boundary layer had reattached; prior to reattachment, the model boundary layer was turbulent at that location. The turbulent model boundary layer caused higher heating, the steel insert's temperature rose more than the surrounding aluminum, and it was still cooling at the times of these images. This effect is visible in several images (e.g., Figure 17), but is clearest here.

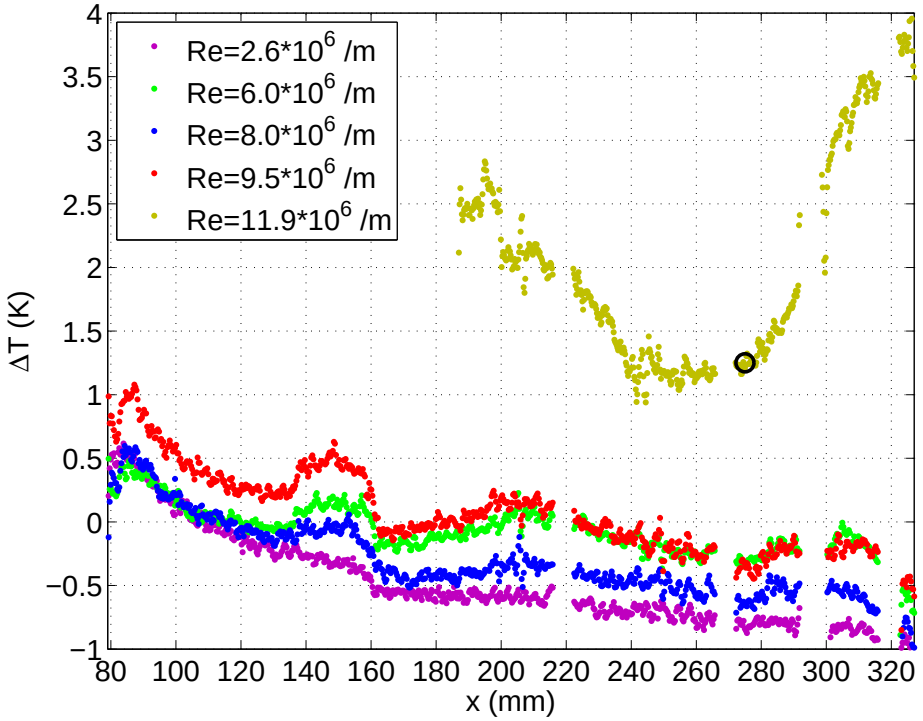

Figure 26: Centerline temperatures for $\alpha = 4°$ under quiet flow

Under noisy flow, the effect of Re at $\alpha = 4°$ is comparable to the effect at $\alpha = 0°$ (Figure 27). The shape of the transition front is consistent and it moves upstream at higher Re. Centerline transition is ahead of crossflow at $\alpha = 4°$. At $Re = 2.8 \cdot 10^6$ /m, only centerline transition is present.

The trend of transition moving closer to the nosetip as Re increases is apparent in Figure 28, the streamwise temperature profiles from the images in Figure 27. The temperature profiles show the classic trend — temperature decreases slowly as x increases until transition onset, where T increases rapidly until reaching a maximum where turbulence is fully developed, and then shows another slow decrease as the turbulent boundary layer thickens.

Table 3 summarizes the transition locations assessed from Figures 25, 27, and 28 using the method described previously. The results are comparable to those at $\alpha = 0°$ (Table 2). The 2.2× delay under quiet flow for $Re = 11.9 \cdot 10^6$ /m is the delay between noisy flow and the flow suspected to be quiet. Once again, there may be some influence of tunnel noise on transition this far downstream in the nozzle.

Table 3: Summary of centerline transition locations for $\alpha = 4°$

Re	Location (mm)		Transition Re_x ($\cdot 10^6$)		Transition Delay
($\cdot 10^6$ /m)	Quiet	Noisy	Quiet	Noisy	quiet Re_x/ noisy Re_x
2.6–2.8	> 328	190	> 0.85	0.53	> 1.6
6.0–6.1	> 328	170	> 2.0	1.0	> 1.9
8.0–8.1	> 328	145	> 2.6	1.2	> 2.2
9.5	> 328	140	> 3.1	1.3	> 2.3
11.9	275	125	3.3	1.5	2.2

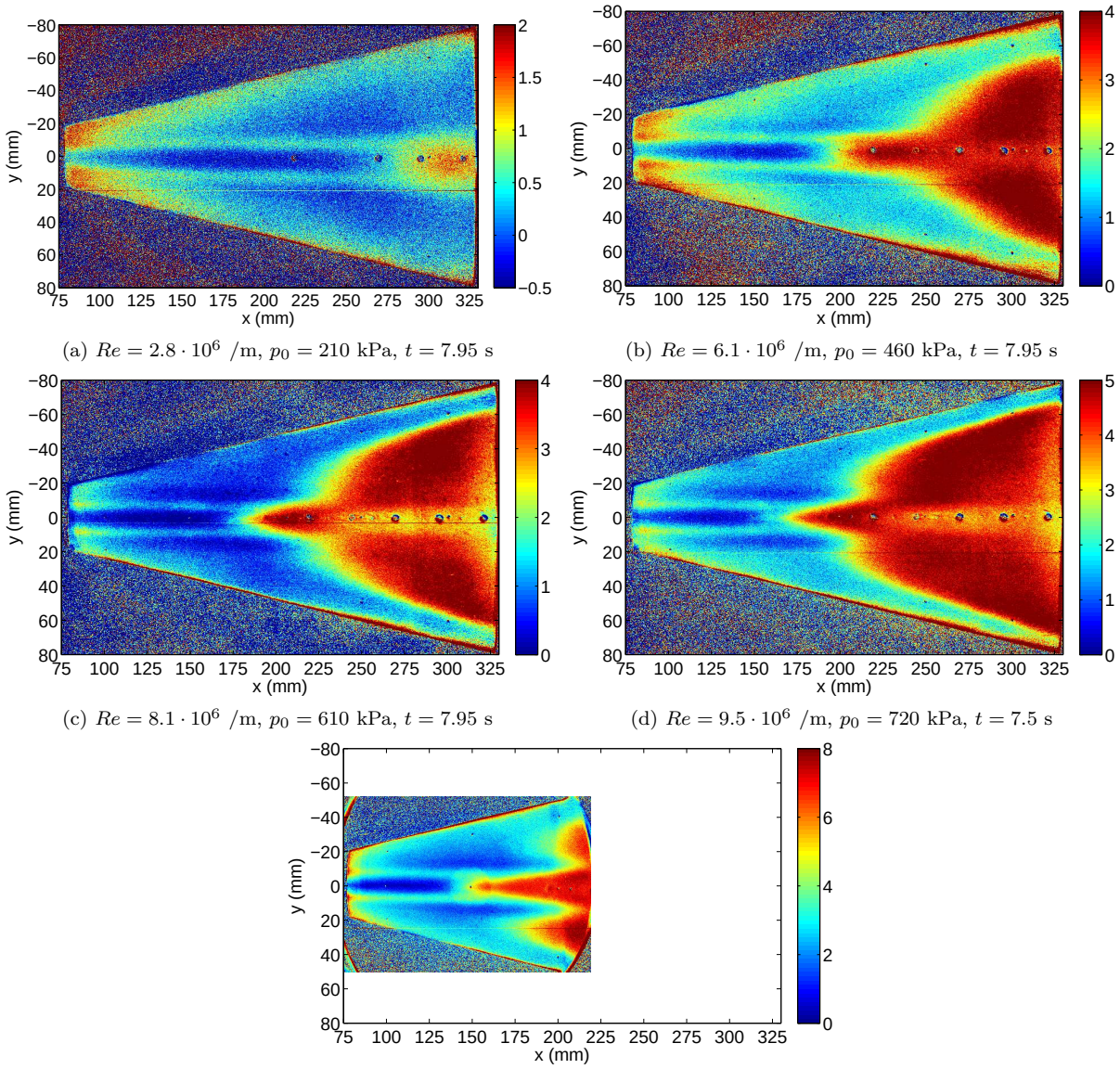

(a) $Re = 2.8 \cdot 10^6$ /m, $p_0 = 210$ kPa, $t = 7.95$ s

(b) $Re = 6.1 \cdot 10^6$ /m, $p_0 = 460$ kPa, $t = 7.95$ s

(c) $Re = 8.1 \cdot 10^6$ /m, $p_0 = 610$ kPa, $t = 7.95$ s

(d) $Re = 9.5 \cdot 10^6$ /m, $p_0 = 720$ kPa, $t = 7.5$ s

(e) $Re = 11.9 \cdot 10^6$ /m, $p_0 = 950$ kPa, $t = 4.5$ s

Figure 27: Effect of varying freestream Re. Noisy flow, $M = 5.8$, $\alpha = 4°$

E. Effect of Surface Finish (Distributed Roughness)

The painted finish on the HIFiRE-5 model necessarily changed the surface roughness from that of a machined aluminum or steel model. Reference 34 describes fruitless attempts to measure the centerline transition front using coaxial thermocouples mounted flush to the model surface.

A significant error was committed in the preliminary analysis of HIFiRE-5 TSP data. In the first data set, the nozzle-wall boundary layer had separated for a large proportion of each quiet-flow run. The pipe insert was installed in the sting-support section, but the pipe insert extension had not yet been fabricated and installed. This configuration resulted in short run times (3–5 s for quiet flow) and confusing hot-film readings. The separated nozzle flow went undetected until June 2009 when the pipe insert extension was installed. When comparing temperature contours on the HIFiRE-5 under separated and attached nozzle flow, a dramatic difference in transition location was seen — but it was wrongly attributed to the model finish, not rejected because it arose from unacceptable flow quality.

A careful reexamination of earlier data found 0.6 s of attached, quiet flow in one run with the orange-peel finish. Figure 29 is a comparison of TSP data from that run with a later smoother-finish paint under

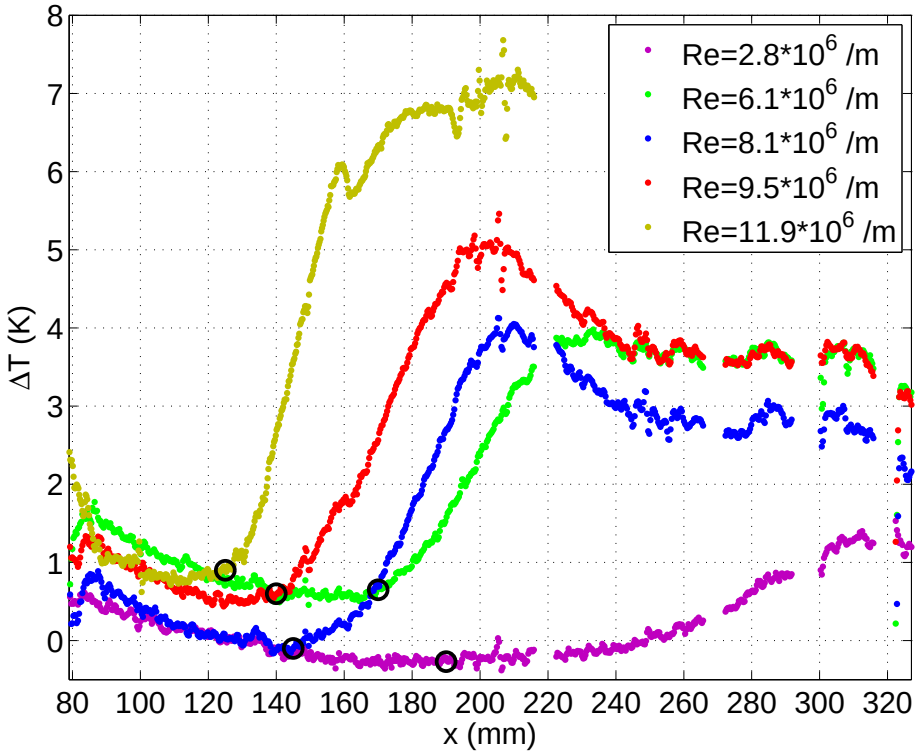

Figure 28: Centerline temperatures for $\alpha = 4°$ under noisy flow

otherwise similar conditions. The profilometer found root-mean-square surface finishes of 0.17–0.42 μm for the 'smooth' finish. All TSP data in this report except Figure 29b has the 'smooth' finish. It is unclear whether and where transition occurs for the rough finish. Transition is not apparent on the centerline for the orange-peel finish, but the aft portion of the model ($x > 290$ mm) was not painted. Because centerline transition cannot be discerned clearly with the rough finish, no conclusion regarding centerline transition can be made.

Crossflow transition or elevated heating from crossflow vortices is present for the rough finish, however. For the smoother finish, crossflow streaks are visible and remain distinct to back edge of model. Elevated heating occurs in the same spanwise location for both, but the rise becomes larger farther upstream for the rough finish. It is thus concluded that the roughness promoted the amplification of crossflow vortices, but no quantitative conclusion can be drawn. The ΔT range in Figure 29b is much larger because the original insulator (INI Nansulate) has a lower thermal conductivity than the LustreKote spray paint.

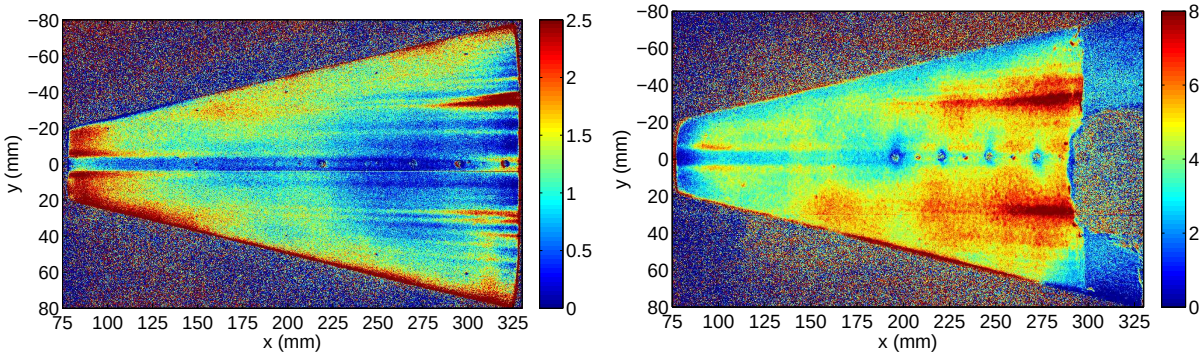

(a) 'Smooth' finish, $Re = 10.2 \cdot 10^6$ /m, $p_0 = 940$ kPa

(b) Orange peel finish, $Re = 10.0 \cdot 10^6$ /m, $p_0 = 920$ kPa

Figure 29: Effect of surface finish. Quiet flow, $M = 6.0$, $\alpha = 0°$

Figure 30 shows the spanwise temperature profiles at $x = 280$ mm for the two contour plots in Figure 29. At this downstream location, both images show temperature peaks at $y = \pm 30$ mm. However, for the rough finish, the peak is much larger relative to the baseline level. This difference suggests that transition is further advanced for the rough finish.

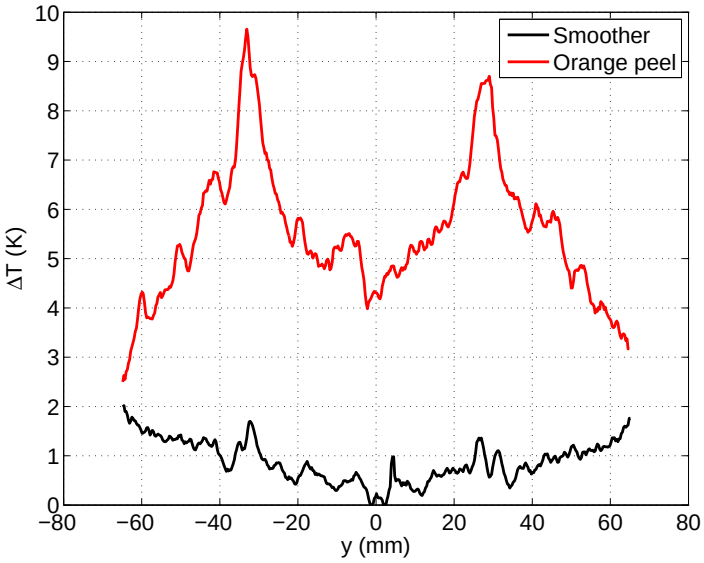

Figure 30: Effect of surface finish on spanwise temperature profile. Quiet flow, $M = 6.0$, $\alpha = 0°$, $x = 280$ mm

F. Effect of Forward-Facing Step

The effect of reducing the forward-facing step at the nosetip/frustum junction ($x = 76.2$ mm) is illustrated in Figure 31. As shown in Figure 10, the step is not eliminated entirely but rather the paint was sanded so that its thickness increases more gradually. The paint was tapered over a length of about 6 mm. The overall temperature distributions, and in particular the location of centerline transition onset and hot streaks induced by crossflow vortices, are essentially the same. It is thus concluded that the difference between the steeper step and the smoother fairing of the paint at that location does not substantially affect the boundary layer stability at these flow conditions. On the basis of this similarity, results with the unsanded step are considered comparable to subsequent tests with the edge smoothed. The data from high-pressure runs presented herein (any images through the porthole windows) were collected with the unsanded paint edge. Except for Figures 31a and 29b, all TSP images through the large window are with the tapered paint edge.

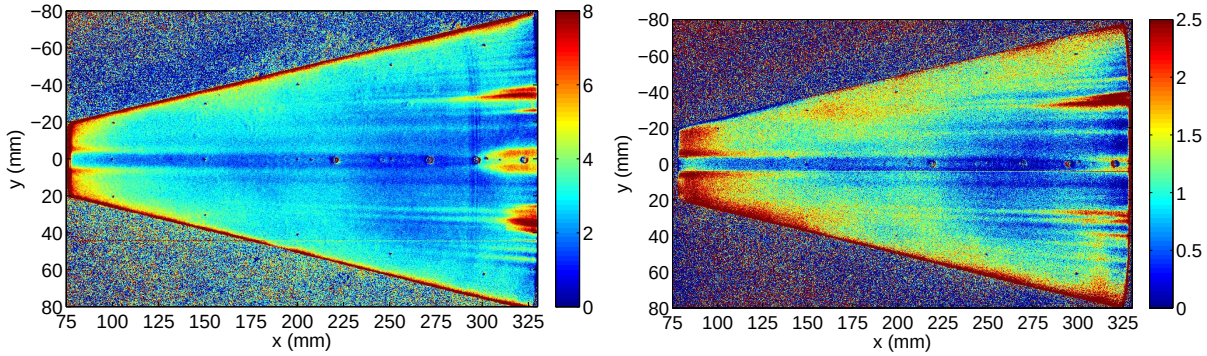

(a) Original untapered step, $Re = 10.3 \cdot 10^6$ /m, $p_0 = 950$ kPa

(b) Reduced step, $Re = 10.2 \cdot 10^6$ /m, $p_0 = 940$ kPa

Figure 31: Effect of forward-facing step at $x = 76$ mm. Step profiles are presented in Figure 10. Quiet flow, $M = 6.0$, $\alpha = 0°$, $T_0 = 429$ K, $t = 0.5$ s

The scale differs significantly between the two subfigures in Figure 31. It was surprising that the temperature range would be so different for these two runs — the test conditions are the same, and the paint was not changed. The test with the sanded step was conducted about two months after the earlier tests, which was made one month and several high-pressure runs after the paint was originally applied. The model was stored in its carrying case to prevent extended exposure to light. The difference is probably due to the natural decay in TSP sensitivity.

IX. Measurement of Boundary-Layer Instabilities with Fast Pressure Sensors

A. PCB Fast-Response Pressure Transducers

The use of PCB fast-response piezoelectric pressure transducers in the BAM6QT is a fairly recent development, first accomplished by Estorf and developed further by Casper.[45–47] The analysis and interpretation of their output is still a work in progress at this facility.[48] These sensors were first employed to measure second-mode disturbances by Fujii.[49]

The sensors were designed as time-of-arrival sensors, so they produce accurate frequency measurements within a large range — 11 kHz to 1 MHz. The factory-provided calibrations unique to each sensor were used to convert the output voltage to pressure. Compared to frequency measurements, the magnitude calibration is somewhat questionable. Efforts to dynamically calibrate these sensors are ongoing.[50] For this reason, the growth of disturbances was not computed, but will only be discussed qualitatively.

B. Normalization of PCB Data

After the PCB voltage was converted to pressure with the factory calibration, these fluctuation magnitudes were normalized by the mean wall pressure as computed by Meelan Choudhari. Dr. Choudhari extracted the pressure from the LAURA computations described in Reference 25. The conditions simulated were: freestream $M = 6.0$, $p_0 = 970$ kPa, $T_0 = 433$ K, $Re = 10.2 \cdot 10^6$ /m, and model wall $T = 300$ K. Table 4 lists the values of p_{wall} that were used.

Table 4: Computed mean wall pressures used in PCB normalization

	mean p_{wall} (kPa)	
x (mm)	$\alpha = 0°$	$\alpha = 4°$
220	1.369	2.054
270	1.369	2.053
320	1.366	2.053

For other conditions, it was assumed that the mean wall pressure is proportional to the stagnation pressure, so p_{wall} was multiplied by $p_0(t)/970$ (where 970 kPa is p_0 for the computed case). The power spectral density was calculated on a signal with dimensions of p'/p_{wall}, where p' signifies that the PCB signal is the fluctuating component of the pressure.

C. Computation of Power Spectral Density

A frequency spectrum analysis of PCB data was performed to determine which disturbance frequencies are amplified within the boundary layer. Because these naturally-occurring disturbances are continuous in the frequency domain, power spectral densities were computed.[51] A power spectral density (PSD) is a measurement of power per unit bandwidth — [units]^2 per Hz.

A separate PSD was computed for each 0.1-s segment of PCB data. Longer segments enable more averaging and/or higher frequency resolution, but shorter time segments yields greater uniformity of flow conditions and reduce the probability of interference from a turbulent burst. This duration was chosen as a balance between these two considerations. Because the BAM6QT produces quasi-steady flow in 0.2-s steps, a 0.1-s segment ensures that at most two stagnation pressure steps will be averaged together, and that a careful selection of the window could realize constant freestream conditions.

The base-10 logarithm of the PSD is computed and plotted to improve the visibility of data over several orders of magnitude. One segment of pre-run data (starting at $t = -0.2$ s) is shown to establish a baseline

electronic noise level. PSD are not calculated for the tunnel startup ($-0.1 < t < 0.2$). Data during nozzle-wall boundary-layer separation are similarly omitted. Finally, segments corrupted by the passage of turbulent bursts were deleted. Each curve in a set of power spectra corresponds to 0.1 s of attached flow between startup and shutdown. During the run, the power decreases steadily as the stagnation pressure decreases.

D. Agreement Between TSP and PCB Indications of Transition Under Noisy Flow

For the majority of BAM6QT HIFiRE-5 tests, temperature-sensitive paint data were collected concurrently with the PCBs. The PCB sensor locations ($x = 220$, 270, and 320 mm) are visible in the TSP images. The circle centered at $x = 295$ mm is a Schmidt-Boelter heat-transfer gauge. This setup enables an outstanding opportunity for side-by-side comparison of the TSP and PCB output. Inferring transition from TSP and interpreting PCB power spectra are both works in progress, so these results are not definitive, but they do provide compelling evidence of agreement between the techniques under noisy flow.

1. 4° Angle of Attack

Figures 32 and 33 show TSP and PCB data, respectively, from one run under noisy flow at 4° angle of attack. Figure 32b shows the centerline temperature profile from the global contour in Figure 32a. These data are from the lowest pressure case in Figures 27 and 28. Using the method described in Section VI, the TSP indicates transition onset at $x = 190$ mm. The maximum centerline temperature, which is taken to correspond to fully-turbulent flow, occurs at $x = 310$ mm.

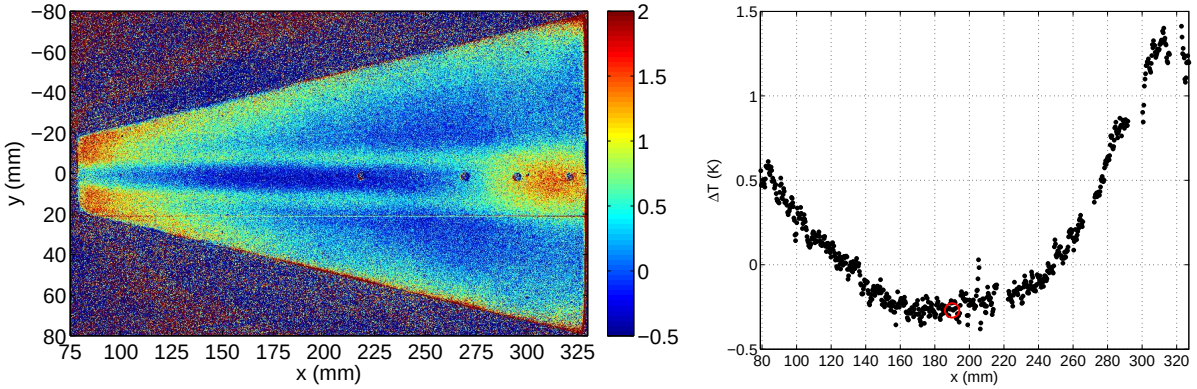

(a) TSP ΔT (K)

(b) Centerline temperature profile. Red circle marks inferred transition onset location

Figure 32: TSP for comparison to PCB power spectra under noisy flow. $M = 5.8$, $\alpha = 4°$, $Re = 2.8 \cdot 10^6$ /m, $p_0 = 210$ kPa, $T_0 = 396$ K, $t = 7.95$ s

The PCB at $x = 220$ mm shows disturbances centered at 100 to 110 kHz with a 60-kHz width, which is suspected to be due to second-mode waves. This sensor's location is 30 mm downstream of the initial temperature rise, but $\partial T/\partial x$ is still very small and the location is well ahead (90 mm) of the end of transition, so it is not surprising that these disturbances are visible in the power spectra. The peak's frequency decreases as stagnation pressure decreases, which is expected.[46,47] Lower stagnation pressure corresponds to lower Reynolds number and a thicker boundary layer, which in turn would have a lower associated second-mode wave frequency. Lower stagnation pressure also implies lower initial disturbance amplitudes. This factor may explain why the peak amplitudes do not collapse when normalized by freestream Reynolds number.

The PCB at $x = 270$ mm shows higher noise levels over a broad range of frequencies, suggesting that the boundary layer is more turbulent (Figure 33b). A hump centered at ≈ 100 kHz is visible, but it does not rise as far above the signal at other frequencies (less than half of an order of magnitude, rather than more than one order). No evidence of the 100 kHz peak is visible in the third PCB ($x = 320$ mm, Figure 33c). This result is consistent with the TSP indication of fully-turbulent flow. The sensor does, however, exhibit a peak at 125 kHz that appears to be an amplification of some noise detected during the pre-run as well.

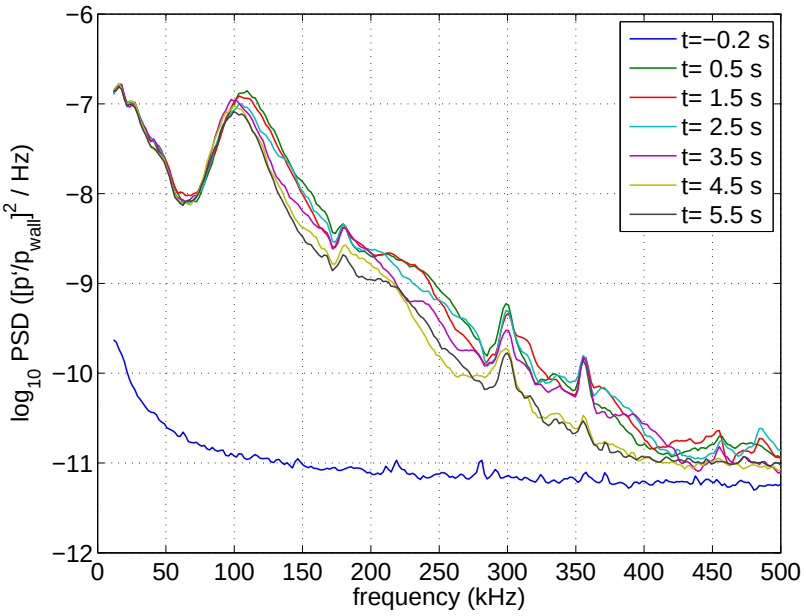

(a) $x = 220$ mm

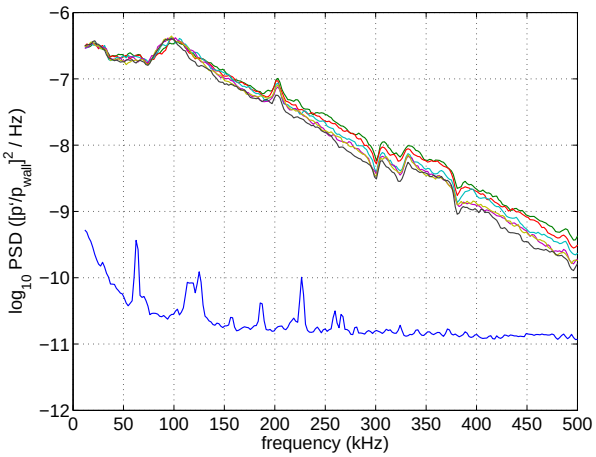

(b) $x = 270$ mm

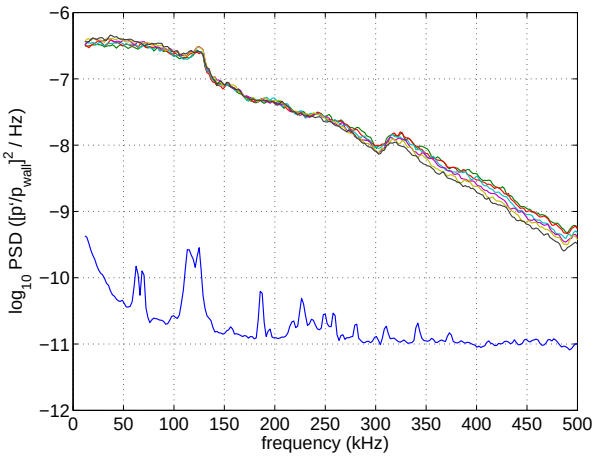

(c) $x = 320$ mm

Figure 33: PCB power spectra under noisy flow. Legend common to all subfigures. $M = 5.8$, $\alpha = 4°$, $Re_i = 3.3 \cdot 10^6$ /m, $p_{0i} = 280$ kPa, $T_{0i} = 433$ K

2. 0° Angle of Attack

Figures 34 and 35 are analogous to 32 and 33 except they show data for 0° instead of 4° angle of attack. Figure 34b shows the centerline temperature profile from the global contour in Figure 34a. These data are from the lowest-pressure case in Figures 23 and 24. The TSP indicates transition onset at $x = 205$ mm. The temperature rise is very gradual and the TSP signal-to-noise ratio is not very good at this low pressure, so the transition location is very hard to judge. Any estimate from 180 to 240 mm seems reasonable, which is an uncertainty of ±15%.

The PCB at $x = 220$ mm (Figure 35a) shows disturbance frequencies of 60–65 kHz. Similar frequencies are detected further downstream at $x = 270$ mm (Figure 35b). According to the TSP data, these sensors both appear to be under a transitional boundary layer. Figure 35b exhibits a large pre-run peak at $f = 62$ kHz, so there is some concern that the peak observed during the run could be affected by noise evident in the prerun signal. However, during the run the peak frequency decreases by about 10%, which meets with the expectation of a thickening boundary layer as Re decreases. For the PCB at $x = 320$ mm (Figure 35c), where the TSP indicates a turbulent boundary layer, the power spectra no longer display the distinct peak

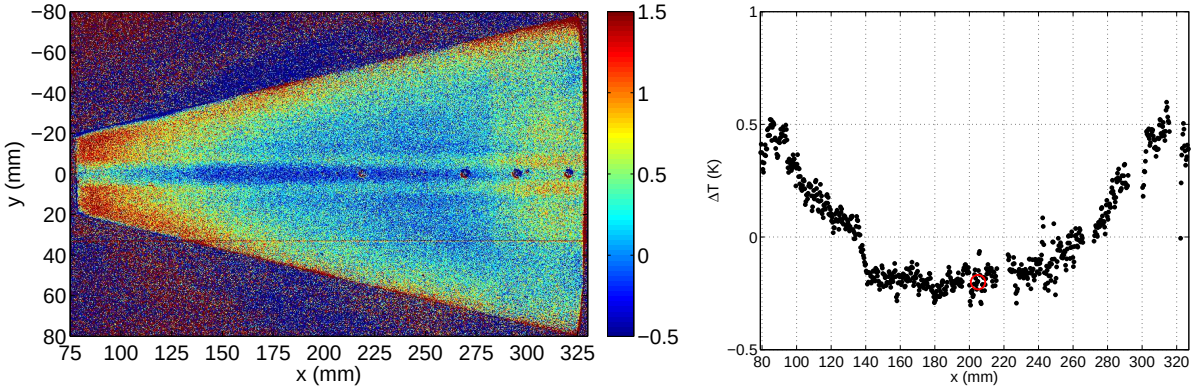

(a) TSP ΔT (K)

(b) Centerline temperature profile. Red circle marks inferred transition onset location

Figure 34: TSP for comparison to PCB power spectra under noisy flow. $M = 5.8$, $\alpha = 0°$, $Re = 2.8 \cdot 10^6$ /m, $p_0 = 210$ kPa, $T_0 = 396$ K, $t = 7.95$ s

at 60–65 kHz. Figure 35c bears a strong resemblance to 33c despite the different angle of attack. The peak at 125 kHz is once again present before and during the run.

For $\alpha = 0°$, the TSP indicates that the boundary layer transitions to turbulent ahead of the first PCB sensor at the other (higher) Reynolds numbers tested. The PCB power spectra exhibit high-amplitude disturbances over a large frequency range. This result is the same as for $\alpha = 4°$.

Dr. Choudhari provided LST computations based on a preliminary mean-flow solution. They are for $Re = 10.2 \cdot 10^6$ /m, higher than the $Re \approx 3 \cdot 10^6$ /m in Figure 35. At $x = 220$, 270, and 320 mm, the highest amplification rates were for disturbance frequencies of 90–100 kHz. If the assumptions are made that the disturbance frequency is inversely proportional to the boundary layer thickness, and that the boundary layer thickness is proportional to $Re^{-1/2}$, then the highest-amplified frequency for $Re = 3 \cdot 10^6$ /m would be roughly 50–55 kHz, which is close to the 55–65 kHz indicated by the PCBs prior to transition.

E. Difficulty of PCB Interpretation Under Quiet Flow

PCB data were collected under quiet as well as noisy flow. These data proved to be much harder to interpret than their noisy-flow analogues, at least partially due to the small magnitudes of the pressure fluctuations encountered. The 125 kHz peak discussed above was mistaken for a disturbance present in the flow before its constancy despite changing angle of attack, Reynolds number, and noise level was realized. It is possible that second-mode waves along the centerline under quiet flow were detected, but at the moment confidence in these results is not high enough for them to be presented. They are discussed further in Reference 34.

X. Summary and Conclusions

Temperature-Sensitive Paint was employed to visualize the temperature rise on the frustum of a 38.1% scale model of the HIFiRE-5 blunt elliptic cone at Mach 6 under quiet and noisy flow. Boundary layer transition was inferred from increases in the streamwise temperature profile. A substantial delay in transition was observed when running with a low noise level. There is concern about the flow quality at the aft end of the BAM6QT test section when running at high stagnation pressure — whether the flow is truly quiet at this location requires further investigation. If the noise level is truly low throughout the test section, then these results are the first evidence in the BAM6QT of transition under quiet flow that is not induced by deliberately-generated roughness. Until now, quiet-flow transition had been detected only on vehicles with isolated roughness elements intended to trip the boundary layer, such as the X-51 and HIFiRE-1. There was a two-fold increase of Re_x at the transition location under quiet compared to noisy flow.

Transition on the HIFiRE-5 appears to arise from amplification of two different modes — second-mode waves along the centerline, and crossflow vortices between the centerline and leading edge. Transition on the windward side along the centerline was delayed slightly ($< 10\%$) when increasing angle of attack from 0° to

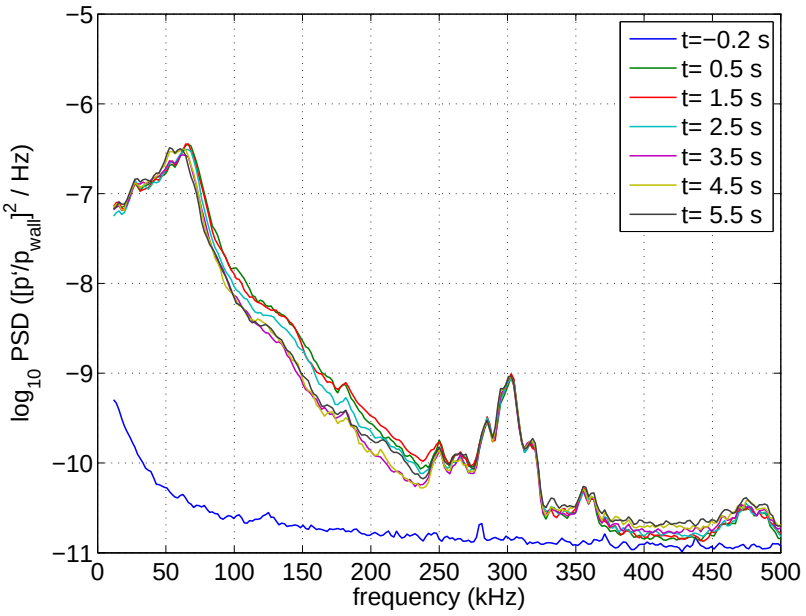

(a) $x = 220$ mm

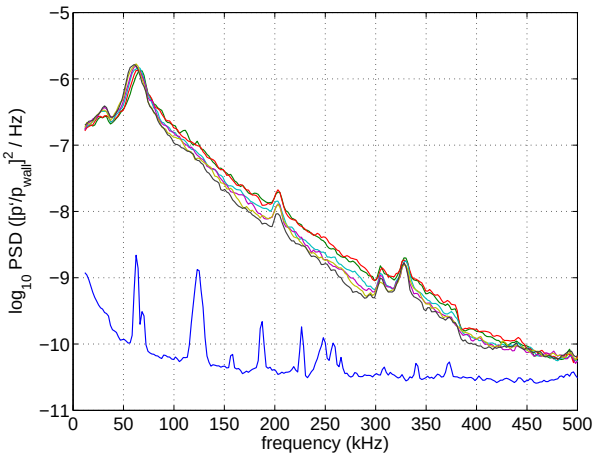

(b) $x = 270$ mm

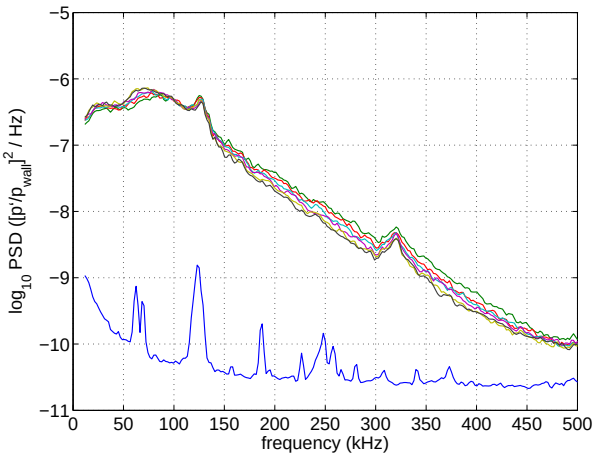

(c) $x = 320$ mm

Figure 35: PCB power spectra under noisy flow. Legend common to all subfigures. $M = 5.8$, $\alpha = 0°$, $Re_i = 3.3 \cdot 10^6$ /m, $p_{0i} = 280$ kPa, $T_{0i} = 433$ K

4° under both quiet and noisy flow. Crossflow transition was delayed substantially at higher angle of attack. This difference is attributed to the reduced spanwise pressure gradient on the elliptic cone as α is increased in this range.

Non-ideal TSP applications were exploited to investigate the effect of surface finish and a forward-facing step. Unfortunately, the original rough 'orange-peel' finish was not characterized well. Compared to the relatively smooth final paint job, the temperature rise presumed to arise from crossflow vortices occurs earlier. Centerline transition is impossible to discern for the rough finish. When a 0.33-mm forward-facing step 76.2 mm from the tip was tapered over a $\approx$ 6-mm distance, no difference in centerline or crossflow transition was detected.

PCB fast-response pressure sensors were used to detect fluctuations in the boundary layer above the centerline prior to transition under noisy flow. The peak frequency was 110–115 kHz at on the windward side at $\alpha = 4°$ and 55–65 kHz at $\alpha = 0°$. The thicker boundary layer at $\alpha = 0°$ probably accounts for this difference. Stability computations at this Re are not available. The PCB data are harder to interpret under quiet flow, probably because of the smaller amplitudes of the fluctuations.

Acknowledgments

This project was funded by the AFOSR under grant FA9550-09-1-0191. Dr. Roger Kimmel (AFRL) provided the HIFiRE-5 geometry and assistance along the way. Dr. Meelan Choudhari (NASA Langley) provided his computational results for comparison.

References

[1]Douglas J. Dolvin. Hypersonic International Flight Research and Experimentation (HIFiRE): Fundamental sciences and technology development strategy. AIAA Paper 2008-2581, April 2008.

[2]C. R. Alba, H. B. Johnson, M. D. Bartkowicz, and G. V. Candler. Boundary layer stability calculations of the HIFiRE Flight 1 vehicle in the LaRC 20-Inch Mach 6 Air Tunnel. AIAA Paper 2008-505, January 2008.

[3]K. T. Berger, F. A. Green, and R. L. Kimmel. Aerothermodynamic testing and boundary layer trip sizing of the HIFiRE Flight 1 vehicle. AIAA Paper 2008-640, January 2008.

[4]K. T. Berger, F. A. Green, R. L. Kimmel, C. R. Alba, and G. V. Candler. Aerothermodynamic testing and boundary-layer trip sizing of the HIFiRE Flight 1 vehicle. *Journal of Spacecraft and Rockets*, 45(6):1117–1124, November–December 2008.

[5]K. M. Casper and B. M. Wheaton. Effect of freestream noise on roughness-induced transition at Mach 6. AIAA Paper 2008-4291, June 2008.

[6]Eli Reshotko. Stability and transition, how much do we know? *U.S. National Congress of Applied Mechanics*, pages 421–434, June 1986. American Society of Mechanical Engineers.

[7]John D. Anderson Jr. *Hypersonic and High Temperature Gas Dynamics*, chapter 6, Viscous Flow: Basic Aspects, Boundary Layer Results, and Aerodynamic Heating. American Institute of Aeronautics and Astronautics, Inc., Reston, VA, 1989.

[8]Steven P. Schneider. Laminar-turbulent transition on reentry capsules and planetary probes. *Journal of Spacecraft and Rockets*, 43(6):1153–1173, November–December 2006.

[9]John Laufer. Aerodynamic noise in supersonic wind tunnels. *Journal of the Aerospace Sciences*, 28(9):685–692, September 1961.

[10]Ivan E. Beckwith. Development of a high Reynolds number quiet tunnel for transition research. *AIAA Journal*, 13(3):300–306, March 1975.

[11]S. R. Pate and C. J. Schueler. Radiated aerodynamic noise effects on boundary layer transition in supersonic and hypersonic wind tunnels. *AIAA Journal*, 7(3):450–457, March 1969.

[12]Steven P. Schneider. Effects of high-speed tunnel noise on laminar-turbulent transition. *Journal of Spacecraft and Rockets*, 38(3):323–333, May–June 2001.

[13]Steven P. Schneider. Development of hypersonic quiet tunnels. *Journal of Spacecraft and Rockets*, 45(4):641–664, July–August 2008.

[14]R. L. Kimmel and J. Poggie. Three-dimensional hypersonic boundary layer stability and transition. Technical Report WL-TR-97-3111, Air Force Research Laboratory, Wright-Patterson Air Force Base, OH 45433-7542, December 1997.

[15]J. Poggie, R. L. Kimmel, and S. N. Schwoerke. Traveling instability in a Mach 8 flow over an elliptic cone. *AIAA Journal*, 38(2):251–258, February 2000.

[16]M. Huntley and A. Smits. Transition studies on an elliptic cone in Mach 8 flow using Filtered Rayleigh Scattering. *European Journal of Mechanics B: Fluids*, 19:695–706, 2000.

[17]Mark B. Huntley. *Transition on Elliptic Cones at Mach 8*. PhD thesis, Princeton University Department of Mechanical and Aerospace Engineering, November 2000.

[18]R. L. Kimmel, M. A. Klein, and S. N. Schwoerke. Three-dimensional hypersonic boundary-layer computations for transition experiment design. *Journal of Spacecraft and Rockets*, 34(4):409–415, July-August 1997.

[19]J. D. Schmisseur, S. P. Schneider, and S. H. Collicott. Receptivity of the Mach-4 boundary-layer on an elliptic cone to laser-generated localized freestream perturbations. AIAA Paper 1998-0532, January 1998.

[20]J. D. Schmisseur, S. P. Schneider, and S. H. Collicott. Supersonic boundary-layer response to optically generated freestream disturbances. *Experiments in Fluids*, 33(2):225–232, August 2002.

[21]Ian J. Lyttle. On the use of transition correlations for three-dimensional boundary layers within hypersonic, viscous flows. Master's thesis, Arizona State University, Mechanical and Aerospace Engineering, August 1994.

[22]S. L. Huang, G. K. Stuckert, and T. Herbert. Cross flow instability of the supersonic flow over a 4:1 elliptic cone. Technical Report 95-0077TR, AFOSR, 1995. DTIC citation AD-A291128.

[23]H. L. Reed and T. S. Haynes. Transition correlations in three-dimensional boundary layers. *AIAA Journal*, 32(5):923–929, May 1994.

[24]Meelan Choudhari et al. HIFiRE5: boundary layer analysis. Private communication; presentation `HF5_preliminary_results_0309.pdf`, March 2009.

[25]M. Choudhari, C.-L. Chang, T. Jentink, F. Li, K. Berger, G. Candler, and R. Kimmel. Transition analysis for the HIFiRE-5 vehicle. AIAA Paper 2009-4056, June 2009.

[26]J. Lukasiewicz. *Experimental Methods of Hypersonics*. Marcel Dekker, Inc., New York, 1973.

[27]T. J. Juliano, E. O. Swanson, and S. P. Schneider. Transition research and improved performance in the Boeing/AFOSR Mach-6 quiet tunnel. AIAA Paper 2007-0535, January 2007.

[28]T. J. Juliano, S. P. Schneider, S. Aradag, and D. Knight. Quiet-flow Ludwieg tube for hypersonic transition research. *AIAA Journal*, 46(7):1757–1763, July 2008.

[29]Thomas J. Juliano. Nozzle modifications for high-Reynolds-number quiet flow in the Boeing/AFOSR Mach-6 Quiet Tunnel. Master's thesis, Purdue University, School of Aeronautics and Astronautics, December 2006. Available from DTIC as ADA456772.

[30]Michael J. Hannon, Jr. Evaluation of diffuser modifications for the Boeing/AFOSR Mach-6 Quiet Tunnel. Master's thesis, School of Aeronautics and Astronautics, Purdue University, August 2008.

[31]B. M. Wheaton, T. J. Juliano, D. C. Berridge, A. Chou, P. L. Gilbert, K. M. Casper, L. E. Steen, and S. P. Schneider. Instability and transition measurements in the Mach-6 Quiet Tunnel. AIAA Paper 2009-3559, June 2009.

[32]C. R. Skoch, S. P. Schneider, and M. P. Borg. Disturbances from shock/ boundary-layer interactions affecting upstream hypersonic flow. AIAA Paper 2005-4897, June 2005.

[33]Craig R. Skoch. *Disturbances from Shock/Boundary-Layer Interactions Affecting Upstream Hypersonic Flow*. PhD thesis, Purdue University School of Aeronautics & Astronautics, December 2005.

[34]Thomas J. Juliano. *Instability and Transition on the HIFiRE-5 in a Mach-6 Quiet Tunnel*. PhD thesis, Purdue University School of Aeronautics & Astronautics, August 2010.

[35]Justin Rubal. Quantitative global heat transfer in a Mach-6 quiet tunnel using temperature sensitive paints. Master's thesis, Purdue University School of Aeronautics & Astronautics, August 2010.

[36]Erick O. Swanson. *Boundary-Layer Transition on Cones at Angle of Attack in a Mach-6 Quiet Tunnel*. PhD thesis, Purdue University School of Aeronautics & Astronautics, August 2008.

[37]T. Liu and J. P. Sullivan. *Pressure and Temperature Sensitive Paints*. Springer-Verlag, 1st edition, 2005.

[38]Justin Rubal. pressure-sensitive TSP. Personal communication (e-mail), February 22 2010.

[39]Leslie M. Mack. Boundary layer linear stability theory. In *Report 709, Special Course on Stability and Transition of Laminar Flow*, pages 1–81. AGARD, March 1984.

[40]W. S. Saric, H. L. Reed, and E. B. White. Stability and transition of three-dimensional boundary layers. *Annual Review of Fluid Mechanics*, 35:413–430, 2003.

[41]W. Saric and H. Reed. Stability, transition, and control of three-dimensional boundary layer on swept wings. In G. E. A. Meier and K. R. Sreenivasan, editors, *IUTAM Symposium on One Hundred Years of Boundary Layer Research*, pages 177–188, 2006.

[42]M. P. Borg, S. P. Schneider, and T. J. Juliano. Effect of freestream noise on roughness-induced transition for the X-51A forebody. AIAA Paper 2008-0592, January 2008.

[43]Matthew P. Borg. *Instability and Transition on the X-51*. PhD thesis, Purdue University School of Aeronautics & Astronautics, August 2009.

[44]D. C. Berridge, A. Chou, C. A. C. Ward, L. E. Steen, P. L. Gilbert, T. J. Juliano, S. P. Schneider, and J. E. Gronvall. Hypersonic boundary layer transition experiments in a Mach-6 quiet tunnel. AIAA Paper 2010-1061, January 2010.

[45]M. Estorf, R. Radespiel, S. P. Schneider, H. B. Johnson, and S. Hein. Surface-pressure measurements of second-mode instability in quiet hypersonic flow. AIAA Paper 2008-1153, January 2008.

[46]K. M. Casper, S. J. Beresh, J. F. Henfling, R. W. Spillers, B. Pruett, and S. P. Schneider. Hypersonic wind-tunnel measurements of boundary-layer pressure fluctuations. AIAA Paper 2009-4054, June 2009.

[47]Katya M. Casper. Hypersonic wind-tunnel measurements of boundary-layer pressure fluctuations. Master's thesis, Purdue University, School of Aeronautics and Astronautics, August 2009.

[48]C. R. Alba, K. M. Casper, S. J. Beresh, and S. P. Schneider. Comparison of experimentally measured and computed second-mode disturbances in hypersonic boundary-layers. AIAA Paper 2010-897, January 2010.

[49]Keisuke Fujii. Experiment of the two-dimensional roughness effect on hypersonic boundary-layer transition. *Journal of Spacecraft and Rockets*, 43(4):731–738, July-August 2006.

[50]Dennis C. Berridge. Measurements of second-mode waves in hypersonic boundary layers with a high-frequency pressure transducer. Master's thesis, Purdue University, School of Aeronautics and Astronautics, December 2010.

[51]David Formenti. Choosing a spectral measurement for data analysis. *Sound and Vibration*, pages 2–3, June 2000.